CSIRO PUBLISHING

International Journal of Wildland Fire **2016**, *25*, 48–61
http://dx.doi.org/10.1071/WF15090

Measuring radiant emissions from entire prescribed fires with ground, airborne and satellite sensors – RxCADRE 2012

Matthew B. Dickinson[A,M], *Andrew T. Hudak*[B], *Thomas Zajkowski*[C,K], *E. Louise Loudermilk*[D], *Wilfrid Schroeder*[E], *Luke Ellison*[F,G], *Robert L. Kremens*[H], *William Holley*[I,L], *Otto Martinez*[I,L], *Alexander Paxton*[I], *Benjamin C. Bright*[B], *Joseph J. O'Brien*[D], *Benjamin Hornsby*[D], *Charles Ichoku*[F], *Jason Faulring*[H], *Aaron Gerace*[H], *David Peterson*[J] and *Joseph Mauceri*[H]

[A]USDA Forest Service, Northern Research Station, 359 Main Road, Delaware, OH 43015, USA.
[B]USDA Forest Service, Rocky Mountain Research Station, Forestry Sciences Laboratory, 1221 South Main Street, Moscow, ID 83843, USA.
[C]USDA Forest Service, Remote Sensing Applications Center, 2222 W. 2300 South Salt Lake City, UT 84119, USA.
[D]USDA Forest Service, Center for Forest Disturbance Science, Southern Research Center, 320 Green Street, Athens, GA 30602, USA.
[E]Department of Geographical Sciences, University of Maryland, College Park, MD 20742, USA.
[F]NASA Goddard Space Flight Center, 8800 Greenbelt Road, Greenbelt, MD 20771, USA.
[G]Science Systems and Applications, Inc., 10210 Greenbelt Road, Suite 600, Lanham, MD 20706, USA.
[H]Rochester Institute of Technology, Center for Imaging Science, 54 Lomb Memorial Drive, Rochester, NY 14623, USA.
[I]US Air Force, 96th Test Wing, Eglin Air Force Base, Niceville, FL 32542, USA.
[J]National Research Council, 7 Grace Hopper Avenue, Monterey, CA 93943, USA.
[K]Present address: Institute for Transportation Research and Education, North Carolina State University, Raleigh, NC 27695, USA.
[L]Deceased.
[M]Corresponding author. Email: mbdickinson@fs.fed.us

Abstract. Characterising radiation from wildland fires is an important focus of fire science because radiation relates directly to the combustion process and can be measured across a wide range of spatial extents and resolutions. As part of a more comprehensive set of measurements collected during the 2012 Prescribed Fire Combustion and Atmospheric Dynamics Research (RxCADRE) field campaign, we used ground, airborne and spaceborne sensors to measure fire radiative power (FRP) from whole fires, applying different methods to small (2 ha) and large (>100 ha) burn blocks. For small blocks ($n = 6$), FRP estimated from an obliquely oriented long-wave infrared (LWIR) camera mounted on a boom lift were compared with FRP derived from combined data from tower-mounted radiometers and remotely piloted aircraft systems (RPAS). For large burn blocks ($n = 3$), satellite FRP measurements from the Moderate-resolution Imaging Spectroradiometer (MODIS) and Visible Infrared Imaging Radiometer Suite (VIIRS) sensors were compared with near-coincident FRP measurements derived from a LWIR imaging system aboard a piloted aircraft. We describe measurements and consider their strengths and weaknesses. Until quantitative sensors exist for small RPAS, their use in fire research will remain limited. For oblique, airborne and satellite sensors, further FRP measurement development is needed along with greater replication of coincident measurements, which we show to be feasible.

Additional keywords: fire behaviour, fire radiative power, MODIS, remote sensing, unmanned aircraft systems, VIIRS, WASP.

Received 11 September 2014, accepted 30 July 2015, published online 23 December 2015

Introduction

Wildland fire radiation measurements are both a central challenge and important opportunity for fire science because they remain poorly validated and yet relate directly to the combustion process and can be obtained remotely over a range of resolutions and spatial extents (Kremens *et al.* 2010). Increasingly, fire radiation measurements have been derived from mid-wave (MWIR) and/or long-wave infrared (LWIR) data obtained from ground-based (e.g. Butler *et al.* 2004; Hiers *et al.* 2009; O'Brien *et al.* 2015) and airborne platforms (Riggan *et al.* 2004; Hudak *et al.* 2015*a*). Fire radiative power (FRP, in MW) has also been retrieved from a growing number of polar-orbiting and geostationary satellite sensors with advanced fire detection capabilities. Recent studies have shown that satellite-retrieved FRP is related to measures of burn severity (e.g. Heward *et al.* 2013) and proportional to fuel consumption and smoke emission rates (e.g. Roberts *et al.* 2005; Wooster *et al.* 2005). Fires with high FRP may also result in an increased chance of smoke injection and transport within the free troposphere (e.g. Val Martin *et al.* 2010; Peterson *et al.* 2014).

Comparisons between coarse- and higher-resolution satellite data (Giglio *et al.* 2003; Wooster *et al.* 2003) and between overlapping pixels from the same satellite sensor (Freeborn *et al.* 2014) offer a means to assess measurement precision. Assessing measurement accuracy requires comparison against a reliable standard that could be provided by airborne and/or ground-based sensors (Peterson *et al.* 2013, 2014; Schroeder *et al.* 2014*a*). An ideal for measurement evaluation would be the existence of reliable ground measurements that would allow validation of airborne measurements and, in turn, reliable airborne measurements that could be used to validate satellite measurements (Kremens *et al.* 2010). Schroeder *et al.* (2014*a*) report a promising concordance of FRP measured by tower-mounted radiometers, spatially coincident FRP measured from an aircraft, and satellite measurements from a single prescribed fire.

Several known limitations affect the precision and accuracy of radiation measurements obtained from satellite, airborne and ground-based radiation sensors. Freeborn *et al.* (2014) and others (e.g. Schroeder *et al.* 2010) identified the fire's location within a large satellite pixel as a major source of error – a phenomenon arising from the non-uniformity of the sensors' point spread function (the change in detector sensitivity from the centre of a pixel to its margin). Point spread function effects have not been incorporated in measurement processes for other sensors, such as single-pixel dual-band radiometers (Kremens *et al.* 2010; 2012). For airborne and satellite measurements, radiation absorption by the intervening atmosphere must be included in the measurement process, given the range in deployment altitude (for airborne sensors) and the range in obliquity of the view angle (Peterson and Wang 2013). Error arising from the use of two limited regions of the infrared (IR) spectrum (usually a MWIR and a LWIR band) in analysis of radiation data (the bi-spectral method) are small under ideal conditions (Peterson and Wang 2013; Peterson *et al.* 2013), but can be large for a variety of reasons, including poor co-registration between bands, differential atmospheric absorption for different bands, small fractional fire areas within (large) pixels and reflected mid-wave solar radiation (Giglio and Kendall 2001; Zhukov *et al.* 2006; Schroeder *et al.* 2010). For highly oblique measurements (e.g. O'Brien *et al.* 2015), the assumption of symmetry of radiation from fires in all directions is critical (e.g. Freeborn *et al.* 2008) – an issue that remains unexplored for spreading fires in the field. Finally, existing calibration approaches assume blackbody/greybody radiation from fires (e.g. Wooster *et al.* 2003; Justice *et al.* 2006; Kremens *et al.* 2010, 2015), ignoring emissions from hot gases (e.g. Dupuy *et al.* 2007).

The 2012 Prescribed Fire Combustion and Atmospheric Dynamics Research (RxCADRE) field campaign allowed for the collection of an integrated dataset of fuels, fire behaviour, fire effects and smoke on a set of small and large fires for the purpose of creating datasets for use in developing and evaluating fire and smoke models. An overview of the specific RxCADRE goals, measurements and study region is provided by Ottmar *et al.* (2015*a*). In this paper, we report on the ground-based, airborne and satellite radiation data obtained during RxCADRE and examine radiation (spatially integrated) over entire prescribed burn units with the goals of developing methods for evaluating satellite measurements (e.g. Coen and Schroeder 2013; Schroeder *et al.* 2014*a*; *b*; Peterson *et al.* 2013; Peterson and Wang 2013; Freeborn *et al.* 2014) and evaluating whole-burn-block fuel consumption estimates (see Hudak *et al.* 2015*a*). This paper draws on information from other papers in this special issue (Hudak *et al.* 2015*a*; O'Brien *et al.* 2015; Ottmar *et al.* 2015; Zajkowski *et al.* 2015). Our description of methods will support future studies using RxCADRE data. Although low replication at the level of burn blocks limits assessments of FRP accuracy and precision, we use the RxCADRE dataset to explore practical issues related to obtaining coincident radiation measurements from different infrared sensors collecting at different scales and to guide a discussion of the challenges in evaluating fire radiation measurements.

Study area, instrumentation and methods

Burns reported in this paper were conducted at Eglin Air Force Base (Eglin AFB) on Range B70 in October and November 2012, and included small (2 ha, $n = 6$) and large (>100 ha, $n = 3$) blocks dominated by herbaceous and shrub fuels and one large forested block (Fig. 1, details in Ottmar *et al.* 2015*a*).

Fire radiation sensors and measurement methods

Sensors and measurement approaches are summarised in Table 1. On small burn blocks where fires were of short duration, we compare FRP derived from an oblique, LWIR camera mounted on a boom lift with those derived from combined data from nadir-viewing, tower-mounted radiometers and remotely piloted aircraft systems (RPAS). For large burn blocks, we report measurements from the Wildfire Airborne Sensor Program (WASP) LWIR sensor flown on a fixed-wing, piloted aircraft and compare those measurements with FRP estimated from two spaceborne sensors: the Suomi–National Polar-orbiting Partnership's Visible Infrared Imaging Radiometer Suite (VIIRS), and the Earth Observing System Moderate-resolution Imaging Spectroradiometer (MODIS) instrument. The WASP measurements have a sufficient spatial extent to capture our large blocks in their entirety but are limited by their return

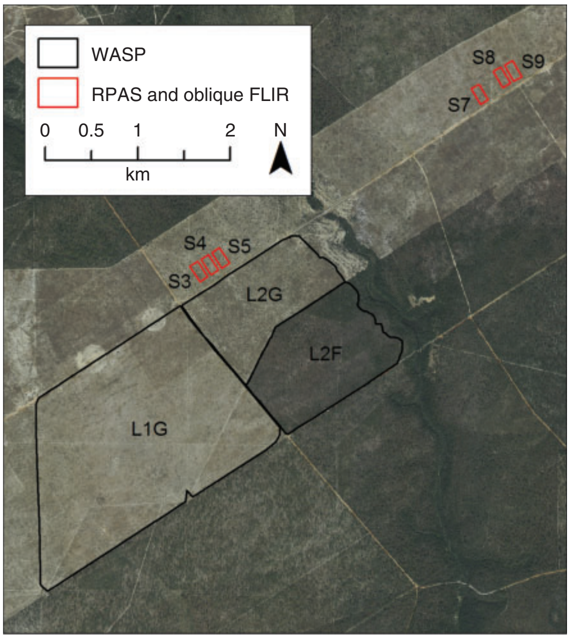

Fig. 1. Small and large burn blocks for which data are presented in this paper. For large burn blocks, fire radiative power (FRP, in MW) was estimated from long-wave infrared (LWIR) data from the Wildfire Airborne Sensor Program sensor flown on a piloted aircraft and from satellite sensors (Moderate-resolution Imaging Spectroradiometer and Visible Infrared Imaging Radiometer Suite (VIIRS)). For small burn blocks, FRP was estimated from a combination of data from dual-band radiometers and a LWIR camera flown on a remotely piloted aircraft system (RPAS). RPAS-based FRP estimates were compared with estimates derived from data from a LWIR camera with an oblique perspective of the fires. Fire in one small burn block (S5) also coincided with a VIIRS overpass. Block L2F was forested whereas the vegetation on the other blocks was a mix of herbs and shrubs.

interval (~3 min) to extent degree that they would not be suitable to characterise the time course of radiation for small blocks. Only on one small block did we obtain three coincident measurements of FRP; these were from a combination of RPAS and ground-based radiometer data, oblique camera and VIIRS.

The different measurement methods we consider all purport to provide comparable values of FRP. That is, the calibration methodologies used extrapolate measurements in limited bandpasses to the relevant portion of the infrared spectrum from which most wildland fire radiation is emitted (roughly 1–20 μm). Given limited replication, we can say little about accuracy, precision and bias – key issues for future measurement campaigns.

Fire radiative power from RPAS and nadir-viewing radiometers

RPAS are receiving increasing interest in fire operations and science applications but experience in their use is limited. The RxCADRE project offered the opportunity to assess capabilities in the context of prescribed fire operations (Zajkowski *et al.* 2015). Here, we report the methods by which whole-fire FRP for small burn blocks was derived using a combination of RPAS and ground-based radiometer data – a combination necessary because of saturation of the FLIR TAU 640 imagery collected from the RPAS. Because of the saturation, it was not possible to discern confidently areas of active combustion from warm ground after the passage of the fire front. The only feature that could be reliably identified in the imagery was the active flame front. Deriving further information from the imagery, such as regions of heading, backing and flanking behaviour, was not possible. Accordingly, FRP was calculated as the product of perimeter length (m) extracted from RPAS imagery and average radiative fireline intensity (RFI, kW m^{-1}) estimated from

Table 1. Details on radiation measurements conducted during RxCADRE 2012

Further information on the FLIR Tau instrument are provided in Zajkowski *et al.* (2015) and on the FLIR instrument in O'Brien *et al.* (2015). The airborne infrared calibration process is described in Accessory publication 1. Details on Moderate-resolution Imaging Spectroradiometer (MODIS) measurements are provided in Accessory publication 2. The aircraft flight altitude was constant within each deployment, though varied among deployments in accordance with burn block width. The remotely piloted aircraft system (RPAS) perimeter length is multiplied by the average radiative fireline intensity (RFI) derived from the ground-based radiometer measurements to yield fire radiative power (FRP). Pixel size for oblique long-wave infrared (LWIR) was determined during post-processing whereas nominal nadir-perspective pixel size is provided for airborne Wildfire Airborne Sensor Program (WASP) and satellite measurements. The focal plane array dimensions of the RPAS and WASP LWIR cameras were 640 × 512 whereas that of the oblique LWIR camera was 640 × 480. Ground dimension refers to either the nominal pixel dimension or radiometer field of view (note units). The satellite sensors are scanners and swath width is, in practice, dependent on the acceptable level of obliquity whereas extent for oblique measurements is poorly defined. AGL, above ground level; VIIRS, Visible Infrared Imaging Radiometer Suite; MWIR, midrange infrared

Measurement	Platform	Perspective	Instrument	Ground dimension	Extent	Nominal bandpass (μm)	FRP estimation method
Fire perimeter (m)	RPAS (180 m AGL)	Oblique	FLIR TAU 640	0.2 m	NA	7.5–13.5	Not calibrated
Radiometer RFI (kW m^{-1})	Tower (5.5 m AGL)	Nadir	Dual-band radiometer	7 m^2	Single 'pixel'	3–5 and 6.5–20	See methods
FRP (MW)	Boom lift (25 m AGL)	Oblique	FLIR SC660 LWIR	1 m	NA	7.5–13	O'Brien *et al.* 2015
FRP (MW)	Aircraft (1550–3160 m AGL)	Nadir	WASP Indigo Phoenix LWIR	1.5–3 m	0.9–1.9 km	8–9.2	Simulation and laboratory calibration
FRP (MW)	EOS/Aqua satellite	Nadir to oblique	MODIS MWIR Channels 22 (high-gain) and 21 (low-gain)	1 km	Scanning	3.93–3.99	~4 μm brightness, Kaufman *et al.* 1998
FRP (MW)	Suomi NPP satellite	Nadir to oblique	VIIRS MWIR Channel I4	375 and 750 m	Scanning	3.55–3.93	MWIR radiance, Wooster *et al.* 2003

replicate radiometer measurements within each burn block. RFI, defined in Smith and Wooster (2005), is the fraction of Byram's fireline intensity (Byram 1959) that is accounted for by radiation.

Nadir-viewing, dual-band radiometers (termed radiometers hereafter) were distributed at 10-m intervals from a central meteorological tower. Radiometer data (Dickinson and Kremens 2015) along with surveyed locations of these instruments are available on the US Forest Service Research Data Archive (Hudak *et al.* 2015). Radiometers were attached to a 0.5-m arm and elevated to 5.5 m on towers constructed of 1.8-m sections of telescoping aluminium tubing (1.47-mm wall thickness; slit ends to facilitate the joining of sections; e.g. see www.dxengineering.com) anchored to steel fence posts. Voltages were logged at 5-s intervals from which fire radiative flux density (FRFD) (W m^{-2}) was calculated (see below). The sensors were built by Dexter Research and are sensitive to different parts of the infrared spectrum. The long-wave sensor (detector ST60 DX-0852) has a silicon window with a nominal bandpass of 6.5–20 μm (spectral transmission described by DC-6186-L2). The mid-wave sensor (detector ST60 DX-0852) has a calcium fluoride window with nominal bandpass of 3–5 μm (spectral transmission described by DC-6100-CaF_2-U8). The field of view of the sensors was 52° at 50% response (i.e. full width at 1/2 maximum response) (FWHM).

Flame front passage through the field of view of a radiometer presents a mixed-temperature scene and complicates raw data calibration (Kremens and Dickinson 2015). The current solution is to incorporate information from both sensors, which, through laboratory blackbody calibration of the ratio of sensor output, allows one to estimate a quantity called the emissivity-area product and, in turn, average FRFD for the area that is emitting radiation above background (pre-fire) levels. Kremens *et al.* (2010) describe the calibration and analysis of dual-band (bi-spectral) radiometer data in detail. See Hudak *et al.* (2015*a*) for measurement evaluation and Kremens *et al.* (2012), Cannon *et al.* (2014) and Kremens and Dickinson (2015) for examples of how radiometer data have been used.

So that whole-fire FRP could be estimated from perimeter information, we needed an estimate of RFI that was as representative as possible of the full depth of the flame front. We assumed that flame fronts were roughly linear as they passed below the radiometers and that flame front width and depth within the field of view of the radiometer were at their maxima when FRFD was at its maximum value. Further, we assumed that flame front width was equal to the diameter of the field of view. The diameter of the field of view was taken to be the diameter at FWHM (5.4 m). Radiometer data are characterised by a rapid rise in FRFD followed by a more gradual decline (Kremens *et al.* 2010). Peak FRFD is likely the result of a composite of radiation from the largest, highest emissivity flames; pyrolysing and glowing fuels; and hot ground (see analysis in Kremens and Dickinson 2015). We assumed that peak FRFD is the best representation of radiation from the entire depth of the flame front, an assumption that should be examined in future work.

Deriving RFI from peak FRFD requires as a first step the multiplication of FRFD by the area of the radiometer pixel that is radiating above background. Neither emissivity nor fire fractional area, components of the emissivity-area (εA) product, could be determined independently from the data at hand so we chose to estimate emissivity as a function of peak FRFD based on an independent dataset described in Bova and Dickinson (2008) and Kremens *et al.* (2012). Placing an upper limit on emissivity of 0.9 and using estimates of flame front area derived from thermocouple arrays and the radiometer field of view (see Bova and Dickinson 2008), we used an iterative process to determine the values of emissivity that minimised the sum of the squared differences between observed and expected fire fractional area. The resulting emissivity estimates were related to peak FRFD as follows ($R^2 = 0.75$):

$$\varepsilon = 0.28(peak\ FRFD)^{0.34}. \tag{1}$$

In turn, emissivity was used to estimate fire fractional area from εA product determined from the RxCADRE radiometer data. Multiplication of fire fractional area by pixel area at FWHM provided an estimate of the area within the pixel that was emitting above background. Peak FRFD was then multiplied by this 'fire area' and divided by the diameter of the field of view to provide RFI. The set of RFI values obtained from replicate radiometer datasets were then averaged for each fire.

Flame front perimeters (m) were described from RPAS LWIR data. Frames encompassing entire blocks were captured by a FLIR Tau 640 camera mounted obliquely on a small RPAS (the fixed-wing G2R, 4-kg maximum takeoff weight) that orbited the block. Specifications of the FLIR Tau camera and G2R aircraft are provided in Table 1 and Zajkowski *et al.* (2015). The frames were orthorectified with reference to infrared 'hot' targets (cans filled with burning charcoal) and features visible on high-resolution aerial orthophotos. The RPAS frames were used to identify flame fronts whose perimeters were manually delineated after image classification. In practice, a consistent camera perspective was needed so that parallax would be constant among successive images of the fires. That is, perimeters were determined only from images captured when the aircraft was at the same point in its orbit limiting the interval between successive perimeter estimates to ~2 min. Parallax was a problem because of orthorectification difficulties (see below). Perimeters were somewhat ambiguous when flame fronts were not continuous, that is, when the flame front extinguished in certain areas. Where the perimeter was not continuous, perimeter segments were summed to estimate total perimeter length.

Fire radiative power from oblique LWIR data

LWIR cameras have been used to provide a nadir perspective of high-resolution flaming combustion for ecological effects research (Hiers *et al.* 2009) but their use to quantify fire dynamics is limited (see Coen *et al.* 2004; O'Brien *et al.* 2015). Here, an uncooled LWIR camera (FLIR model SC660) mounted on a boom lift positioned upwind of the small burn blocks was used to measure fire progression and FRFD from an oblique perspective across the full extent of the blocks (Table 1). Thermal images were captured at 1 Hz, scene emissivity was set at 0.98 and temperature range was set at 300–1500°C. The FLIR systems gave pixel radiometric temperatures in degrees Celsius as raw output. Temperatures were then converted to FRFD using the Stefan–Boltzmann equation for a greybody emitter. Further information on FLIR specifications and image rectification and

Table 2. Fire radiative power (FRP) generated from Moderate-resolution Imaging Spectroradiometer (MODIS) data for the L1G, L2G and L2F burns using different methodologies

See Supplementary material (Accessory publication 2) for a complete characterisation of the methods and their results, which include consideration of pixel selection method and the method by which background FRP was determined. Here, we report the range in values obtained. The lowest value corresponds to the method in which only pixels that were significantly above background were used to generate FRP. The highest value corresponds to that obtained by combining FRP from all pixels that overlapped the burn block thereby including radiation from pixels in which there was limited combustion. There was no saturation in MODIS data and although small burn S6 coincided temporally with MODIS overpass, the signal was lost in the background because of the large scan angle. Large burn L1G was not detected by the MYD14 methodology because of cloud effects and our manual computation of FRP is likely an underestimate. Average atmospheric transmission was used to estimate surface-leaving FRP. Whether a fire was detected (Det.) by algorithm and whether there was signal saturation (Sat.) are indicated. MODIS nadir-perspective pixel size is 1000 m

Fire	Date	Time (UTC)	Scan angle (°)	Pixel area (km^2)	Top of atmosphere power		Surface-leaving (corrected) FRP		Atmospheric absorption (%)	Det.	Sat.
					Pixel	Cluster	Pixel	Cluster			
					(MW)						
S6	31 October	19:43:41	51.2	6.2	NA	NA	NA	NA	NA	N	N
L1G	4 November	19:18:58	27.9	1.5	94.4	94.9	110.4	111.0	17	N	N
L2G	10 November	18:42:01	34.0	2.0	130.1	151.4	153.8	179.3	18	Y	N
L2F	11 November	19:25:05	35.9	2.1	155.6	174.6	187.5	210.6	20	Y	N

processing are found in Hiers *et al.* (2009), Loudermilk *et al.* (2012), and O'Brien *et al.* (2015). Orthorectified image data were rendered at 1-m^2 scale and these data were integrated spatially to provide whole-fire FRP. A 25-m boom lift fully extended and located 10–25 m outside the short side of each block's 100 × 200-m boundary was used to elevate the camera. The perspective to the centre of the burn unit was nominally 85.5° off nadir (compare with a nominal perspective of 84.5° off nadir for Coen *et al.* 2004). The lift was positioned upwind of the burn block (winds were oriented roughly along the long axis of each block) and fires were ignited on the upwind side of the blocks. As such, head fire flame front pixels became increasingly distorted as obliquity increased and resolution decreased with increasing distance between the camera and flame front (for more detail, see O'Brien *et al.* 2015).

Fire radiative power from airborne LWIR data

Airborne infrared imaging can provide data at relatively high spatial resolution over spatial extents typical of operational prescribed fires, thus providing information that can be used to evaluate and understand satellite data (e.g. Schroeder *et al.* 2014*a*). Long-wave imagery was captured by the WASP LWIR camera flown on a twin-engine Piper Navajo, which made repeated passes at about a 3-min interval over each of the three large burns (Table 1 and further details in Hudak *et al.* 2015*a*). Mid-wave infrared data are also available from the WASP system, but saturation and reflected solar radiation limit their use. The WASP system is described in McKeown *et al.* (2004) and its utility is described in Ononye *et al.* (2007). The WASP Indigo Phoenix LWIR camera (model IA126 LWIR) was built by Cantronic Systems Inc. and has quantum well, cooled detectors. Peak transmission is at 8.7 μm, see Table 1 for more details. Flight altitude was determined in part by a tradeoff between the goals of capturing entire blocks in a single mosaic of frames on a single pass and the need to fly below any existing cloud cover.

The general calibration method for obtaining pixel FRFD over the IR spectrum relevant for wildland fires combines laboratory calibration, fire radiation simulations, atmospheric absorption simulations from the Moderate-resolution Atmospheric Transmission code (MODTRAN) (Berk *et al.* 2003) and the spectral response of the camera system, and is described in Kremens and Dickinson (2015, Accessory publication 1). Images were orthorectified using aircraft orientation obtained from an Applanix POS 510 inertial management unit. Camera distortion (internal) models were obtained using the Rochester Institute of Technology IR camera calibration facility. Canopy interception of radiation is a known limitation of both airborne and satellite measurements of fire radiation, but no correction was attempted for our forested block (as compared with Hudak *et al.* 2015). Also, there is some indication that a small amount of fire area was excluded from some mosaics for which we attempted no correction. We expect the quantity to be small because the flight altitude was chosen pre-fire so that the width of frames encompassed entire units and the camera operator monitored the imagery during the flight and guided the pilot's choice of flightline.

FRP from spaceborne sensors

Among the set of active fire imaging sensors, only the daytime (from midday to early afternoon) overpasses from MODIS on the EOS/Aqua satellite and the VIIRS sensor, borne on the S-NPP polar satellite (launched in 2011), were sufficiently available to observe the experimental fires given RxCADRE research priorities and operational constraints. The two satellites follow a similar orbit (Justice *et al.* 2013; Csiszar *et al.* 2014) and their timing is convenient for coordination with prescribed fire operations.

MODIS

The official MODIS fire data product provides datasets of detected fire pixels at 1-km nominal resolution and their respective FRP values calculated only from the ~4-μm brightness temperatures (Table 1, Kaufman *et al.* 1998; Justice *et al.* 2002, 2006; Giglio *et al.* 2003). MODIS overpasses were coincident with experiments S6, L1G, L2G and L2F on 31 October and 4, 10 and 11 November 2012, respectively (Table 2). The MODIS–Aqua active fire product (MYD14)

Table 3. Specification of Visible Infrared Imaging Radiometer Suite (VIIRS) fire radiative power (FRP) retrievals for RxCADRE 2012 fires that coincided with independent FRP measurements

Atmospheric absorption of infrared radiation in the bandpass of the sensors of interest was estimated by Moderate-resolution Atmospheric Transmission code and accounts for sensor spectral response. Because scan angles were sometimes well off nadir, both nominal nadir perspective and actual pixel sizes are provided. The standard deviation associated with VIIRS FRP reflects variation in the multiple pixels used to characterise the background. Whether a fire was detected (Det.) by algorithm and whether there was signal saturation (Sat.) are indicated. Where signal was saturated, FRP was not estimated

Fire	Fire date	Time (UTC)	Nadir pixel resolution (m)	Scan angle (°)	Pixel area (km^2)	Top of atmosphere		Surface-leaving (corrected) FRP		Atmospheric absorption (%)	Det.	Sat.
						Power	s.d. (MW)	Power	s.d.			
S5	1 November	18:15:10	375	41.5	0.28	5.95	0.09	7.96	0.1	25	Y	N
S5	1 November	18:15:10	750	41.5	1.10	4.23	0.70	7.66	1.2	45	N	N
L1G	4 November	18:59:54	375	16.4	0.16	NA	NA	NA	NA	NA	Y	Y
L1G	4 November	18:59:54	750	16.4	0.64	110.30	4.60	158.30	8.6	30	N	N
L2G	10 November	18:47:22	375	3.2	0.14	NA	NA	NA	NA	NA	Y	Y
L2G	10 November	18:47:22	750	3.2	0.56	108.30	4.80	150.80	8.8	28	Y	N
L2F	11 November	18:28:34	375	29.8	0.23	NA	NA	NA	NA	NA	Y	Y
L2F	11 November	18:28:34	750	29.8	0.93	153.70	6.00	236.70	10.3	35	N	N

retrievals for these overpass events were collected and the radiance data were corrected for atmospheric absorption using MODTRAN 4v3 (Berk *et al.* 2003) and atmospheric profiles derived from National Centers for Environmental Prediction 0.5°-resolution 6-hourly data. An average atmospheric absorption weighted by sensor spectral response was used to correct top-of-the-atmosphere values to give ground-leaving FRP (Table 2).

We used the MODIS fire detection process (e.g. Justice *et al.* 2002) to facilitate FRP estimation. Detection is accomplished using the spectral bands centred at ~4 μm (MWIR) and ~11 μm (LWIR), although data from several other spectral bands are also utilised for masking clouds, extremely bright surfaces, glint and other potential sources of false detection (Giglio *et al.* 2003). Fire detections using the MYD14 product were only obtained for the L2G and L2F fires. Two pixels contained fire detections for the L2G plot and four pixels for the L2F plot. However, because of MODIS scanning design and the fact that ground pixel size increases away from nadir, it is possible to have duplicate detections of the same fire as a result of ‘bow-tie’ distortion, which affects pixels acquired at scan angles greater than ~25° (Wolfe *et al.* 2002). This was the case for L2F where two neighbouring scans detected the same fire on the ground. In this case, simply summing the FRP values from both scans would result in an overestimation of overall FRP. Instead, because the first scan only partially detected the fire with one registered fire pixel, the three FRP values from the subsequent scan – which did cover the entire L2F plot – were used to estimate total FRP.

Fires S6 and L1G were coincident with MODIS image acquisition but not detected (Table 2). MODIS’s view angle for burn S6 was highly oblique (51.2°), whereas the active fire area was small (much less than the 2-ha burn block’s area) relative to the pixel’s 6.2-km^2 footprint (Table 2). Consequently, the fire’s radiative signal was too weak to be separated from the background. Inspection of the MYD14 metadata coinciding with L1G showed that the corresponding fire signal was discarded due to the detection of opaque clouds over the L1G fire. FRP for L1G was calculated manually and included in Table 2 with the proviso that the resulting FRP value for L1G will likely underestimate true FRP.

Because the burn block boundaries were known, we were able to place lower and upper bounds on FRP. The lower bound is the summation of individual pixel values that were detected (i.e. were sufficiently above background). The upper bound is the summation of FRP from all pixels that overlapped unit boundaries. A detailed discussion of methods is provided in the Supplementary material (Accessory publication 2), available online only.

VIIRS

VIIRS is a multi-spectral instrument launched in 2012 to support Earth weather and climate applications. Full global coverage is accomplished every 12 h or less using two distinct sets of spectral channels at 375- (Schroeder *et al.* 2014*b*) and 750-m nominal resolution. A unique data aggregation scheme was applied to the sensor’s radiometric data to limit pixel area increase along scan, thereby resulting in greater image integrity compared with other wide-area orbital scanning systems (Wolfe *et al.* 2013). The 750-m dataset includes a dual-gain MWIR channel with a high saturation temperature of 634 K designed to detect and characterise active fires (Table 1, Csiszar *et al.* 2014).

VIIRS imaged S5, L1G, L2G and L2F during active fire spread (Table 3). Automated active fire detection data were produced for the 375- and 750-m datasets using the methodologies described in Schroeder *et al.* (2014*b*) and Csiszar *et al.* (2014), respectively. The 375-m active fire product detected all four fires, whereas the 750-m product detected only the L2G fire. The omission errors in the 750-m product were mainly caused by the small size of the S5 fire resulting in weak radiative signal in the primary MWIR detection channel, and scattered opaque clouds over L1G and L2F causing partial fire obscuration with consequent classification of the area as cloud covered. Because of the low saturation temperature (367 K) of the 375-m MWIR channel driving that active fire algorithm, the larger fires at L1G, L2G and L2F resulted in saturated pixel radiances (Table 3). Meanwhile no pixel saturation was found in the higher saturation temperature (634 K) 750-m data.

To overcome the limitations imposed by fire omission errors and pixel saturation described above, VIIRS 375- and 750-m coincident data were used interchangeably (Table 3).

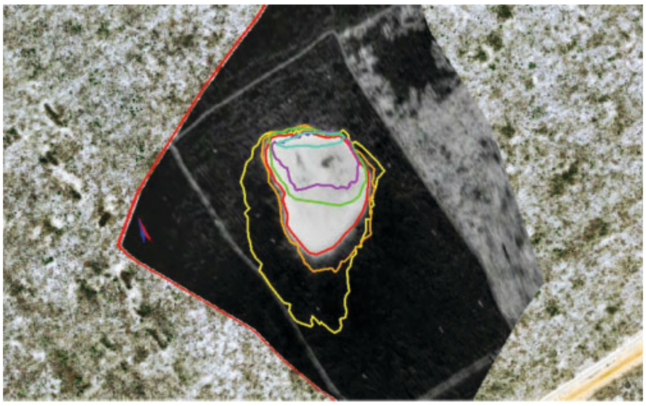

Fig. 2. Remotely-piloted aircraft system (RPAS) long-wave infrared (LWIR) image from the FLIR Tau camera at 18:15:40 Coordinated Universal Time (UTC) for fire in burn block S5 overlain with successive perimeters and underlain by a high-resolution orthophoto. North is up in the image and the dimensions of the burn unit (the light outline encompassing the perimeters) are 100 × 200 m. Surveyed infrared targets are visible within the perimeter with white being relatively hot and black being cool. The RPAS captured images used to extract perimeters from a southerly perspective at 183 m above ground level. Shown are successive perimeters drawn from infrared images at 18:10:28 (teal), 18:13:05 (purple), 18:13:30 (green), 18:15:40 (red), 18:17:59 (orange) and 18:22:49 (yellow).

Table 4. Fire radiative power (FRP) derived from remotely piloted aircraft system (RPAS) imagery (perimeters) and radiometer data (radiative fireline intensity, RFI) for fires in non-forested, small burn blocks

RFI values are averages from either $n = 3$ (S3, S7), $n = 4$ (S5, S9) or $n = 5$ (S4, S8) radiometers. Blocks S3–S5 burned on 1 November 2012 whereas S7 and S9 burned on 8 November 2012. Burn block S6 was not flown and it was not possible to extract perimeter data from S8 imagery

Fire	Time (UTC)	Perimeter (m)	RFI (kW m^{-1})	FRP (MW)
S3	21:29:21	1197	28.5	34.1
S4	19:38:07	204	4.2	0.8
S4	19:40:22	258	4.2	1.1
S4	19:42:44	303	4.2	1.3
S4	19:46:00	446	4.2	1.9
S4	19:50:06	454	4.2	1.9
S4	19:52:32	565	4.2	2.4
S5	18:10:28	114	26.3	3.0
S5	18:13:05	188	26.3	5.0
S5	18:13:30	212	26.3	5.6
S5	18:15:40	298	26.3	7.8
S5	18:17:59	317	26.3	8.3
S5	18:19:23	416	26.3	11.0
S5	18:20:34	402	26.3	10.6
S5	18:22:49	462	26.3	12.2
S7	17:29:02	562	57.7	32.4
S9	18:37:15	294	37.2	10.9

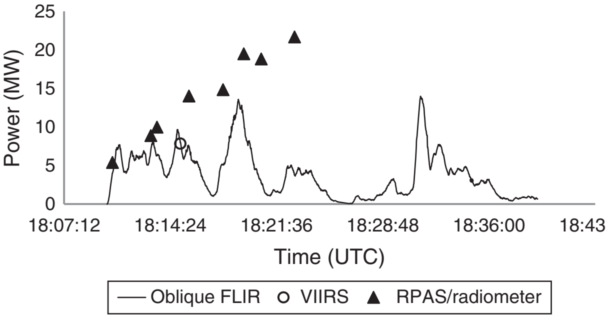

Fig. 3. Whole-fire fire radiative power (FRP) derived from oblique long-wave infrared data for block S5. The second peak coincides with burnout around the downwind perimeter after the main heading fire had approached the unit boundary. Also shown are FRP estimates derived from Visible Infrared Imaging Radiometer Suite data and combined data from remotely piloted aircraft system (RPAS) and ground-based radiometers. The rise in FRP from RPAS and radiometer data is coincident with increasing measured fire perimeter (Table 4).

Fire-affected pixels omitted by the 750-m product were accounted for using co-located reference pixels detected by the 375-m product. Pixel-based FRP retrievals were derived using the method of Wooster *et al.* (2003) applied to unsaturated MWIR (single-band) radiance data only (Table 1). Hence, two separate FRP retrievals were produced using the 375- and 750-m data for block S5, whereas single retrievals based on 750-m radiance data were produced for blocks L1G, L2G, and L2F. VIIRS MWIR radiance data were corrected for atmospheric attenuation using the MODTRAN code as described above.

Results and discussion

FRP from RPAS and nadir-viewing radiometers

An example set of RPAS-derived perimeters is shown in Fig. 2. Estimates of FRP from RPAS and ground-based radiometers are shown in Table 4 along with fire perimeter and RFI. FRP values are subject to uncertainty because of limitations imposed by RPAS imagery and radiometer data. As an illustration, 4 out of 27 radiometer datasets could not be used because retrieved εA products at peak FRFD were non-physical (>1). We suspect that our radiometer calibration, which involves using a blackbody, oversimplifies the spectrum of radiant emissions emanating from real fires that also include hot gas emission in the characteristic wavebands of combustion products (e.g. Boulet *et al.* 2011). Hot gas emissions are nonetheless detected by the sensors because of their wide bandpasses.

Variability in FRP within a given fire is only caused by changes in perimeter length because estimates of RFI were averaged across all radiometers and that average was applied to all perimeter estimates from a given fire (see Table 2); the consequence can be seen in Fig. 3 and Table 4 where FRP increases through time as perimeter length increases. Given the lack of a monotonic increase in FRP in the corresponding oblique FLIR data (Fig. 3), the increase in FRP in the RPAS/radiometer data would appear to be an artefact of our inability to distinguish heading, backing and flanking behaviour (which change in their relative proportions through time) and apply to these different behaviours an appropriate RFI value.

A clear limitation of using small RPAS for fire research is the low quality of both the infrared imagery and the navigation data required to rectify the imagery. Because IR cameras currently available for small RPAS are designed to detect low-temperature objects (e.g. humans), they saturate at the high radiant flux

Table 5. Fire radiative power (FRP) estimates from oblique long-wave infrared (LWIR) images of fires in small burn blocks
The oblique images were obtained from a FLIR camera mounted on a 25-m boom lift. Final image resolution was 1 × 1 m after orthorectification. Total area burned includes all pixels that exceeded a background threshold of 300 K

Burn	Active flaming duration (min)	Mean (s.d.) number of pixels with fire (m^2)	Total area burned (ha)	FRP (MW)	
				Mean (s.d.)	Max
S3	26	324 (286)	2.16	4.2 (3.8)	15.4
S4	20	88 (86)	0.50	1.2 (1.4)	5.5
S5	29	289 (203)	1.14	3.9 (3.0)	14.0
S7	29	150 (217)	1.14	2.1 (3.3)	18.8
S8	23	353 (356)	2.31	5.1 (6.7)	41.7
S9	17	177 (173)	1.82	2.0 (2.0)	7.8

densities associated with fires. Another limitation is that the images captured by the RPAS camera exhibited blooming because (1) the microbolometer array is uncooled, (2) the detectors are not thermally isolated, (3) the 1/30th-s exposure time allows for smearing associated with movement and (4) the LWIR bandpass (8–14) is wide and includes areas of the spectrum in which hot gases in the plume may emit substantial radiation. Rectification of the imagery was made difficult by error in roll, pitch, yaw and position (*xyz*) data from the RPAS, the oblique viewing angle and the lack of sufficient tie points in the thermal imagery around and inside the burn unit (Fig. 2, see Zajkowski *et al.* 2015).

FRP estimated from oblique LWIR data

FRP measured from oblique (rectified) LWIR imagery (Table 5) showed temporal (e.g. Fig. 3) and spatial fluctuations that appeared to be caused by variation in wind speed and direction, and fuels (see O'Brien *et al.* 2015; Rowell *et al.* 2015). In contrast to our RPAS/radiometer measurements of whole-fire FRP that were sensitive only to changes in fire perimeter, the oblique-looking FLIR SC660 is able to detect fluctuations in pixel FRFD and, thus, has value for exploring issues such as spatial and temporal variations in fuel consumption rates. O'Brien *et al.* (2015) considered whether the oblique radiation may have been obscured by intervening fuels but they expect that any effect will be small because the camera was positioned upwind of fires that consumed fuels that otherwise might have obscured the signal. Radiation received by the oblique LWIR camera on the L2F block was obscured by intervening tree foliage and trunks, rendering of little use our single-perspective data as a basis for comparison with the airborne sensor.

FRP estimates from airborne LWIR data

The time courses of FRP for fires in large burn blocks generated from airborne LWIR data are shown in Fig. 4. Peak FRP was higher and the duration of the ignition operations and heat release from the fire occurred over a longer period for the forested block (L2F) than for the non-forested blocks (L1G and L2G). Estimates of background radiative flux density (RFD) from radiometers were used to establish a background threshold for FRP calculation. Background RFD, averaging 1070 W m^{-2} (95% confidence interval (CI) 863–1288 W m^{-2}), was the asymptote approached by RFD after flame fronts spread below instruments (for more information, see Hudak *et al.* 2015*a*). Cloud cover estimated from airborne visible imagery ranged from 0 to 10% for L1G, averaging <5%, and likely reduced airborne FRP estimates.

FRP estimates from spaceborne sensors

Ground-leaving FRP estimates from MODIS (corrected for atmospheric absorption) are shown in Table 2 and with FRP calculated from airborne LWIR data in Fig. 4. A range of estimates were obtained for each fire based on different ways of treating the background and whether flagged fire pixels or clusters of pixels that overlapped the burn blocks were used as the basis for FRP determination (see Supplementary material, Accessory publication 2). The MODIS pixel grid for L2F is shown in Fig. 5 over the most coincident WASP mosaic. Images showing cloud cover at the time of L1G retrieval are shown in the Supplementary material (Accessory publication 2). Note that MODIS FRP measurements are known to have large error bounds associated with the pixel point spread function, and these error bounds can be reduced by averaging values from many pixels (Freeborn *et al.* 2014). As such, we cannot draw statistical conclusions from our few replicate fires. Cloud cover likely reduced the MODIS estimate of FRP for L1G and was ~5% of the burn block at the time of MODIS overpass as estimated from near-coincident WASP imagery.

Ground-leaving FRP estimates from VIIRS data for the three large fires ranged from 151 to 237 MW (Table 3). VIIRS pixels included in the FRP estimate for L2F overlay a near-coincident WASP mosaic in Fig. 5. Scan angles ranged from 3 to 30° off nadir. All three large fires were detected from the 375-m nadir resolution data (realised pixel area of 0.1–0.3 km^2). The fire at site L2G was the only one detected by the coarser 750-m data at near-nadir observation conditions (3.2° scan angle) and 0.56-km^2 effective pixel area. Small fire S5 coincided with a VIIRS overpass and was detected by the 375-m data at a 41.5° scan angle at 350-m nadir resolution with no saturation. For L1G at the time of VIIRS overpass, cloud cover estimated from WASP imagery was ~2% of the burn block (Table 6).

Comparisons among FRP measurements

Coincidence in FRP and timing among airborne LWIR and satellite measurements is shown in Figs 4 and 6 and Table 6. Temporal coincidence was ≤119 s. Comparisons are qualitative because of low replication. For the L1G (MODIS and VIIRS) and L2F (VIIRS) fires, cloud cover was present and may have

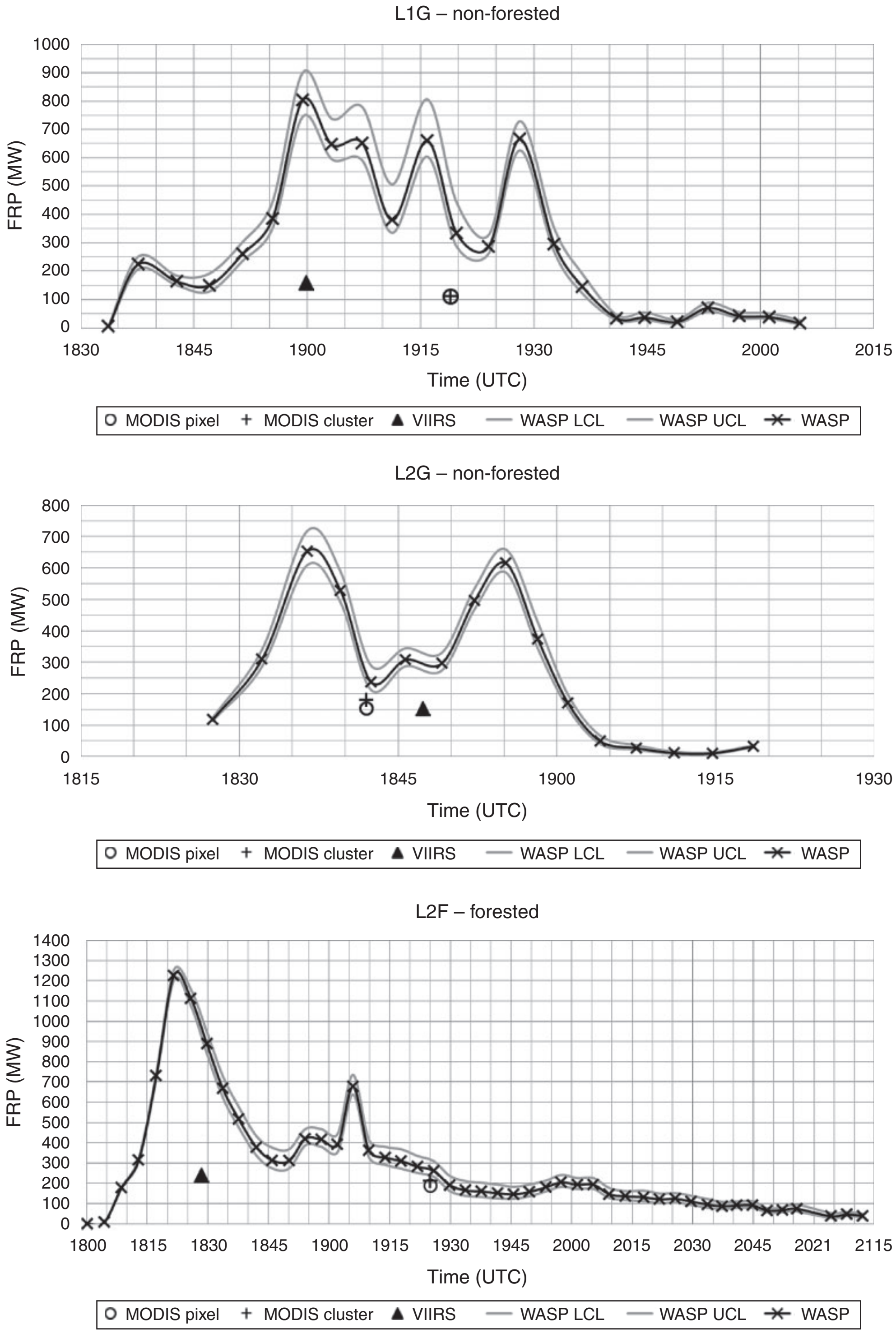

Fig. 4. Time-course of whole-fire fire radiative power (FRP) derived from Wildfire Airborne Sensor Program (WASP) long-wave infrared (LWIR) imagery and associated satellite measurements. Temporal autocorrelation (Table 6) was estimated from these data and from oblique LWIR data shown in Fig. 2. For WASP FRP, shown is the value based on a background threshold of 1070 W m^{-2} and values derived from its upper (863 W m^{-2}) and lower (1288 W m^{-2}) 95% confidence limits (see Hudak *et al.* 2015*a*). Satellite measurements are within 2 min of the closest WASP measurements (Table 6). FRP for L1G for both Moderate-resolution Imaging Spectroradiometer (MODIS) and Visible Infrared Imaging Radiometer Suite (VIIRS) and L2F for VIIRS is expected to be underestimated due to partial cloud obscuration. Pixel and cluster methods for MODIS FRP estimation are described in the Supplementary material (Accessory publication 2).

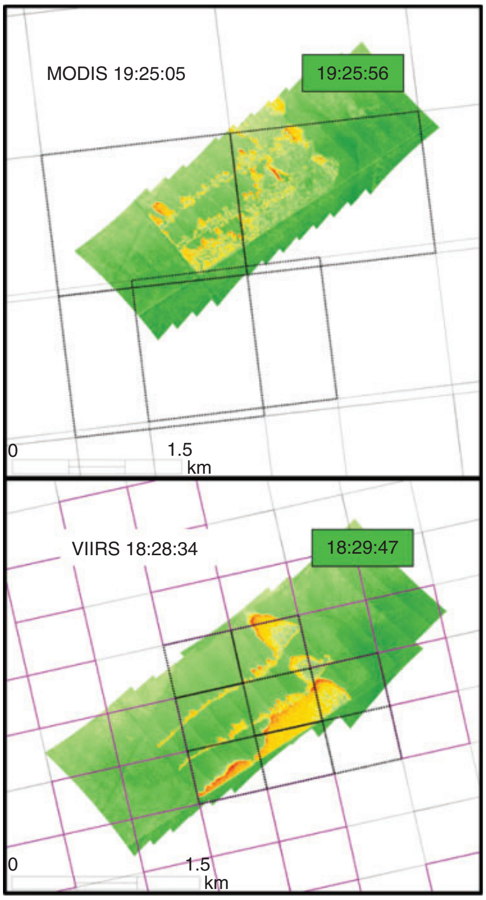

Fig. 5. Near-coincident Wildfire Airborne Sensor Program (WASP) long-wave infrared (LWIR) mosaic (background green–red) overlain by Moderate-resolution Imaging Spectroradiometer (nominal 1000 m) and Visible Infrared Imaging Radiometer Suite (nominal 375 m) active fire masks for burn block L2F. Satellite pixels are displayed according to fire algorithm output classification (thick/dashed = fire detections; magenta = clouds; thin/solid = clear land pixel). Note that the WASP mosaic may miss some heat from near the upper block boundary. All figures show the WASP infrared mosaic that was closest in timing (shown) to the satellite overpass.

Table 6. Fire radiative power (FRP) estimated from airborne LWIR data from the Wildfire Airborne Sensor Program (WASP) system and near-coincident (*a*) Moderate-resolution Imaging Spectroradiometer (MODIS) and (*b*) Visible Infrared Imaging Radiometer Suite (VIIRS) data

The timing of each measurement is provided along with differences in timing and FRP between airborne and spaceborne sensors. The MODIS FRP value is the average of FRP estimated from pixel and cluster methods (see Table 3). An estimate of burn block cloud cover from WASP imagery is available for L1G satellite overpasses. The piloted aircraft was lower than the cloud base during L2F so no estimate of cover was made

(*a*) MODIS

Fire	FRP (MW)			Cloud	Time (UTC)		
	WASP	MODIS	Diff		WASP	MODIS	Diff (s)
L1G	333	111	222	Yes (5%)	19:19:47	19:18:58	49
L2G	238	167	71	No	18:42:26	18:42:01	25
L2F	261	199	62	No	19:25:56	19:25:05	51
		Mean (s.d.)	119 (90)			Mean (s.d.)	42 (14)

(*b*) VIIRS

Fire	FRP (MW)			Cloud	Time (UTC)		
	WASP	VIIRS	Diff		WASP	VIIRS	Diff (s)
L1G	803	158	645	Yes (2%)	18:59:24	18:59:54	30
L2G	297	151	146	No	18:49:08	18:47:22	106
L2F	888	237	651	Yes	18:29:47	18:28:34	73
		Mean (s.d.)	481 (290)			Mean (s.d.)	70 (38)

attenuated radiation reaching the VIIRS and MODIS sensors. Despite attempts at RxCADRE 2012 and before, we have not been able to successfully use ground calibration where a well-characterised heat source is used to calibrate airborne imagery. At RxCADRE 2012, we burned charcoal beds of 1-m diameter, but correlations between airborne and radiometer measurements were unsatisfactory, likely because of noise associated with aggregating WASP pixel data. If correlation had been successful, airborne data could have been validated or calibrated using ground data and, then, satellite data evaluated against airborne data. With larger beds, the radiation would also be measureable directly by satellite, based on the experience of one of the authors (W. Schroeder).

The relationship between FRP estimated from a combination of RPAS and ground-based radiometer data and comparable estimates derived from oblique LWIR was highly variable (Fig. 7). The relationship in Fig. 7 is strongly influenced by the largest RPAS/radiometer estimates of FRP (based on single perimeters from S3 and S7). Increasing perimeter length and, therefore, FRP estimates through time for S4 and S5 (Table 2 and Fig. 3) suggest that without an ability to at least assign different values of RFI to heading, backing and flanking fires, FRP derived from RPAS perimeter data will remain suspect. Saturated RPAS data precluded its use for more than perimeter estimates. Further, blooming of the RPAS imagery may have resulted in inflated perimeter estimates and, thus, FRP for high-intensity fires. Replication of radiometer measurements (*n* of 3 to 5) was low for small blocks, which must increase error and uncertainty for RPAS-based estimates of FRP. Though we have used 20 radiometers on a single burn in past years, the need to distribute a limited set of instruments across three small blocks on any given day limited replication in 2012.

The oblique IR camera would appear to be the better option for quantifying FRP on small burn blocks or portions of large burns though accuracy needs to be examined (see below). The oblique IR estimates of FRP may be biased downward because the LWIR bandpass misses the majority of flame radiation, which has peak emissions in the MWIR region of the IR spectrum (Kremens and Dickinson 2015). Alternative calibration approaches that are more appropriate for wildland fire radiation need to be developed and applied (see example in Kremens and Dickinson 2015).

A general source of downward bias for all radiation measurements reported in this paper may be that, although greybody/

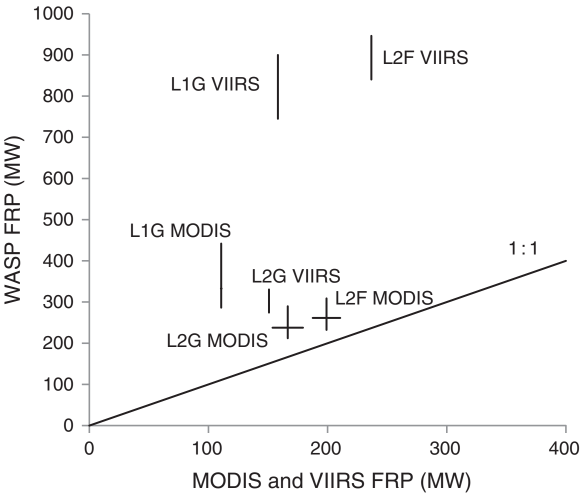

Fig. 6. Comparisons of Moderate-resolution Imaging Spectroradiometer (MODIS) and Visible Infrared Imaging Radiometer Suite (VIIRS) estimates of fire radiative power (FRP) with the estimate from Wildfire Airborne Sensor Program (WASP) long-wave infrared data closest to it in timing. The 1:1 reference line is provided. The range in MODIS measurements from the pixel and cluster methods is shown along the *x*-axis (see Table 2). The range for L1G is small because cloud cover prevented all pixels that overlapped the burn block from being included in the cluster FRP estimate. Both MODIS and VIIRS measurements are corrected for atmospheric absorption. The 95% confidence interval in WASP measurements is shown on the *y*-axis (see Fig. 4). MODIS and VIIRS measurements for L1G and the VIIRS measurement for L2F were affected by clouds.

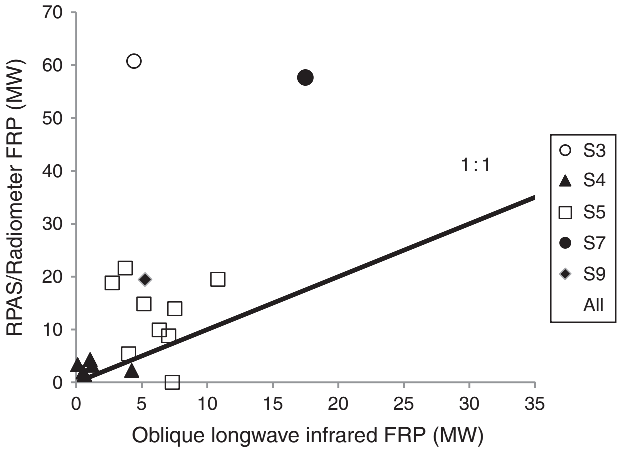

Fig. 7. Comparison of oblique long-wave infrared and remotely piloted aircraft system (RPAS) and radiometer estimates of fire radiative power (FRP) emitted from fires in small burn blocks. Oblique long-wave infrared data were collected from a boom lift outside the fire perimeter. To obtain FRP, fire perimeters (m) derived from RPAS imagery were multiplied by the block-average radiative fireline intensity (kW m^{-1}) estimated from dual-band radiometer data (Table 4). The 1:1 reference line is provided.

blackbody radiation is supported from measurements in high-transmission regions of the infrared spectrum (e.g. Johnston *et al.* 2014), measurements of spectral radiant emissions from fires suggest that radiation from hot flame gases must be considered (e.g. Dupuy *et al.* 2007; Boulet *et al.* 2011). The radiometers and the oblique LWIR camera are perhaps most prone to uncertainty because the radiation they receive includes wavelengths affected by hot gas emissions and absorption by intervening gases whereas their calibration assumes blackbody/greybody radiation. The airborne WASP LWIR passband and MODIS and VIIRS MWIR passbands are little affected by hot gas emission and atmospheric absorption (e.g. Dupuy *et al.* 2007). All radiation measurements in this paper are based on blackbody/greybody assumptions and might be considered speculative to the extent that wildland fire radiation deviates from those assumptions (e.g. Boulet *et al.* 2011). Development of sensors and measurement processes are clearly needed, potentially including the greater use of bi- and multi-spectral data (see VIIRS methods, above; Riggan *et al.* 2004; Kremens *et al.* 2010).

Although we do not believe that a 'gold standard' wildland fire radiation measurement has been implemented in the field, a potential standard by which to assess fire radiation measurements is fuel consumption. We suggest that, where possible, radiation measurements should be time integrated to provide fire radiative energy, converted to fuel consumption through estimates of fire radiative fraction and fuel heat of combustion, and compared with fuel consumption data. Hudak *et al.* (2015*a*) use the range in fire radiative fraction (0.13–0.22) measured in independent experiments in different (mixed-oak) fuels (see Kremens *et al.* 2012) and literature values of heat of combustion to predict fuel consumption at local and burn block scales from radiometer data and oblique and airborne LWIR imagery. Predicted fuel consumption is compared with (observed) fuel consumption derived from pre- and post-fire fuel loads (Ottmar *et al.* 2015*b*). Consumption predicted from radiometer data are close to observed consumption ($n = 16$, mean observed minus predicted is 0.06 Mg ha^{-1} with a 95% CI of 0.04–0.08 Mg ha^{-1}). Average observed consumption was 1.13 Mg ha^{-1} higher than predicted from oblique FLIR data ($n = 6$, 95% CI of 1.12–1.14 Mg ha^{-1}). Excluding L2F, an outlier because of presumed undersampling of duff and downed-woody materials (Hudak *et al.* 2015*a*), observed consumption extrapolated to whole burn units was 1.57 Mg ha^{-1} greater than consumption predicted from airborne LWIR data ($n = 4$, 95% CI of 1.55–1.59 Mg ha^{-1}). Two additional fires from 2011 were also included in this comparison. Clearly, a key science need is to better characterise wildland fire heat budgets generally because fuel consumption predictions depend on estimates of radiative fraction and heats of combustion (Kremens *et al.* 2012).

Our experience corroborates Riggan *et al.* (2004) and Schroeder *et al.* (2014*a*) that coordinating ground, airborne and satellite measurement can be successful. Greater replication of coordinated satellite and airborne measurements has been demonstrated by Peterson *et al.* (2013) who were able to use high-resolution airborne data to validate fire fractional area for $n > 30$ MODIS pixels. In our study, MODIS and VIIRS overpasses were coincident with fires in all three large burn blocks. Coordinating small block firing operations with satellite overpass was successful for two fires (S5 and S6) despite the fact that such coordination was not a high priority in the overall measurement campaign. Though S6 FRP did not rise above MODIS background radiative power, the S5 measurements of 7.3 and 8.0 MW from oblique LWIR and VIIRS, respectively,

Table 7. Temporal autocorrelation in whole-fire fire radiative power (FRP) measurements calculated from oblique long-wave infrared (LWIR) and Wildfire Airborne Sensor Program (WASP) airborne LWIR data

Average FRP is calculated across all replicates. The time lag is the longest lag for which FRP is significantly autocorrelated

Data source	Burn	*n*	Mean time lag (min) (and s.d.)	Average FRP (MW)
Oblique	Small burns	6	1.2 (0.4)	3.1
WASP	Large burns	3	17.3 (4.2)	240.6

coincided closely (Fig. 2). Clouds likely reduced three satellite FRP estimates. Had coincidence with satellite overpass been a top priority, we would have had added flexibility in choosing burn days that were substantially cloud free.

Temporal autocorrelation in FRP

The longest significant lag over which FRP measurements were temporally autocorrelated was determined for each oblique and airborne LWIR dataset using SAS 9.4 PROC TIMESERIES (SAS Institute Inc. 2013). Significant (non-zero) autocorrelation was determined if the 95% CI surrounding the autocorrelation function did not include zero. FRP from whole burns was positively autocorrelated at temporal scales that increased from small (~1 min) to large (~17 min) burn blocks (Table 7). Csiszar and Schroeder (2008) suggest that measurements from different satellite platforms should be within 10 min of each other for Amazonian fires and within 30 min for Boreal fires. Peterson *et al.* (2013) used a 15–17-min window for comparing airborne with MODIS measurements for wildfires in the western US.

By examining oblique FLIR (Fig. 3) and WASP data (Fig. 4) in the context of a 1- and 17-min lag, respectively, it is apparent that significant autocorrelation is a weak standard for measurement coincidence and we expect that an acceptable lag will be smaller than a lag determined by the standard of statistical significance. In this study, the difference in timing between measurements derived from different instruments was always much shorter than the longest significant time lag. For instance, there was no more than a 1-s difference between oblique infrared and RPAS fire perimeters because oblique IR measurements were obtained at high frequency. Temporal coincidence between airborne LWIR and satellite estimates of FRP were <106 s (Table 6 and Fig. 7). For block S5, oblique IR and VIIRS measurements were coincident to within a second.

Deployment considerations

Given the knowledge of satellite orbits, it is possible to plan months in advance when a set of satellites will be in an ideal position to image a prescribed fire. It is more difficult to have an aircraft on hand and ready to fly with the appropriate sensor for reasons of cost, weather and sensor availability. Nevertheless, we were able to obtain concordance between satellite overpass and active burning for the three large fires as well as for two of the six small fires. We suggest that having study sites with large numbers of annual burn days coupled with an aggressive prescribed fire programme is essential for obtaining high replication. Given its weather and successful fire management programme, a place like Eglin AFB has much to recommend it as a site for conducting a highly replicated study. Coordination with military training operations is perhaps the greatest constraint.

For small burns, we found that deployment of the oblique LWIR camera was relatively efficient (see O'Brien *et al.* 2015). The cost of renting the boom lift was modest and the fact that it could be driven from burn unit to burn unit was a major plus. A downside is that a camera operator was required, which would be a concern for certain types of fuels and weather scenarios. A remote triggering system would mitigate risk if that risk were of concern. Critical were the placement of IR targets (pots filled with smouldering charcoal) at surveyed locations within the scene for use as ground control points for orthorectification. Based on comparison with consumption data and analysis by Dupuy *et al.* (2007), a revised calibration process (e.g. Kremens and Dickinson 2015) is required for this camera system.

Though RPAS were successfully integrated into the RxCADRE measurement campaign (Zajkowski *et al.* 2015), we cannot recommend the use of low quality and non-quantitative IR sensors, and small RPAS that do not provide navigation data of sufficient quality for efficient image orthorectification. The difficulty in obtaining images of sufficient quality to extract perimeters resulted in poor replication for some fires, particularly those with high FRP (Fig. 7). Though small RPAS have promise for imaging fires at high temporal and spatial resolution, that promise was not met in this study.

Conclusions

In this paper, we describe the ground-based, airborne and satellite radiation measurements conducted during RxCADRE 2012, discuss their deployment in a prescribed fire operational setting, and examine radiation spatially integrated over entire burn blocks. We found that small RPAS have some utility for characterising flame front development in small burn blocks but their use will remain severely limited without quantitative IR sensors and better three-dimensional position data for image orthorectification. Comparison with RxCADRE fuel consumption data, perhaps the best standard for comparison available currently, increases our confidence in fire radiation measurements from radiometers, but the oblique and airborne IR sensors underpredict measured consumption. Otherwise, oblique cameras have substantial merit in operational imaging of small fires or parts of large fires in non-forested sites, and could be coordinated with airborne imaging. Improving confidence in the use of IR data to derive accurate and precise estimates of FRP requires a better fundamental understanding of wildland fire spectral radiation and its incorporation into the development of measurement devices and calibration processes, a conclusion that applies to all sensors (ground, airborne and satellite) used in this study. Development of methods by which to use radiometer data as a validation and calibration source for airborne and satellite data remains a critical need. RxCADRE field campaigns suggest that future studies focussed on comparative radiation measurements have high potential for success, particularly where good burning weather and successful prescribed fire programmes align.

Acknowledgements

We thank the Eglin AFB fire management staff, particularly Kevin Hiers, Brett Williams and the fire crews for their supreme competence in prescribed burning and logistical coordination. We also thank the many scientists and support staff not included in this paper whose work and collaboration made the RxCADRE project possible, particularly Roger Ottmar who led the effort and Dan Jimenez who facilitated agreements and funding. It is with sadness and gratitude that we note the loss of Dr Otto Martinez and Mr. Bill Holley of the Eglin AFB Digital Video Laboratory. Otto and Bill were central to the planning and implementation of the complex RxCADRE airborne operations and, in addition, they coordinated RPAS operations that included multiple platforms and managed real-time data collection and display. The 2012 RxCADRE campaign was made possible by a grant from the Joint Fire Science Program (Project #11–2-1–11), and longer-term support from the US Forest Service, National Fire Plan, Joint Fire Science Program and NASA was critical for getting the RxCADRE project started. Thanks to Ellen Eberhardt and several anonymous reviewers for their input on the manuscript.

References

Berk A, Anderson GP, Acharya PK, Hoke M, Chetwynd J, Bernstein L, Shettle EP, Matthew MW, Alder-Golden SM (2003) MODTRAN4 version 3 revision 1 user's manual. (Air Force Research Laboratory: Hanscom AFB, MA).

Boulet P, Parent G, Collin A, Acem Z, Porterie B, Clerc JP, Consalvi JL, Kaiss A (2011) Experimental investigation of radiation emitted by optically thin to optically thick wildland flames. *Journal of Combustion* **2011**, 137437. doi:10.1155/2011/137437

Bova AS, Dickinson MB (2008) Beyond 'fire temperatures': calibrating thermocouple probes and modeling their response to surface fires in hardwood fuels. *Canadian Journal of Forest Research* **38**, 1008–1020. doi:10.1139/X07-204

Butler BW, Cohen J, Latham DJ, Schuette RD, Sopko P, Shannon KS, Jimenez D, Bradshaw LS (2004) Measurements of radiant emissive power and temperatures in crown fires. *Canadian Journal of Forest Research* **34**, 1577–1587. doi:10.1139/X04-060

Byram GM (1959) Combustion of forest fuels. In 'Forest fire: Control and Use' (Ed. KP Davis) pp. 61–89 (McGraw Hill: New York, NY).

Cannon JB, O'Brien JJ, Loudermilk EL, Dickinson MB, Peterson CJ (2014) The influence of experimental wind disturbance on forest fuels and fire characteristics. *Forest Ecology and Management* **330**, 294–303. doi:10.1016/J.FORECO.2014.07.021

Coen JL, Schroeder W (2013) Use of spatially refined satellite remote sensing fire detection data to initialize and evaluate coupled weather–wildfire growth model simulations. *Geophysical Research Letters* **40**, 5536–5541. doi:10.1002/2013GL057868

Coen J, Mahalingam S, Daily J (2004) Infrared imagery of crown-fire dynamics during FROSTFIRE. *Journal of Applied Meteorology* **43**, 1241–1259. doi:10.1175/1520-0450(2004)043<1241:IIOCDD>2.0.CO;2

Csiszar IA, Schroeder W (2008) Short-term observations of the temporal development of active fires from consecutive same-day ETM+ and ASTER imagery in the Amazon: implications for active fire product validation. *IEEE Journal of Selected Topics in Applied Earth Observations and Remote Sensing* **1**, 248–253. doi:10.1109/JSTARS.2008.2011377

Csiszar IA, Schroeder W, Giglio L, Ellicott E, Vadrevu KP, Justice CO, Wind B (2014) Active fires from Suomi NPP Visible Infrared Imaging Radiometer Suite: product status and first evaluation results. *Journal of Geophysical Research* **119**, 803–816. doi:10.1002/2013JD020453

Dickinson MB, and Kremens RL (2015) RxCADRE 2008, 2011, and 2012: Radiometer data. Forest Service Research Data Archive (Fort Collins, CO). doi:10.2737/RDS-2015-0036

Dupuy JL, Vachet P, Maréchal J, Meléndez J, de Castro AJ (2007) Thermal infrared emission–transmission measurements in flames from a cylindrical forest fuel burner. *International Journal of Wildland Fire* **16**, 324–340. doi:10.1071/WF06043

Freeborn PH, Wooster MJ, Hao WM, Ryan CA, Nordgren BL, Baker SP, Ichoku C (2008) Relationships between energy release, fuel mass loss, and trace gas and aerosol emissions during laboratory biomass fires. *Journal of Geophysical Research: Atmospheres* **113**, D01301. doi:10.1029/2007JD008679

Freeborn PH, Wooster MJ, Roy DP, Cochrane MA (2014) Quantification of MODIS fire radiative (FRP) measurement uncertainty for use in satellite-based active fire characterization and biomass burning estimation. *Geophysical Research Letters*. doi:10.1002/2013GL059086

Giglio L, Kendall JD (2001) Application of the Dozier retrieval to wildfire characterization: a sensitivity analysis. *Remote Sensing of Environment* **77**(1), 34–49. doi:10.1016/S0034-4257(01)00192-4

Giglio L, Descloitres J, Justice CO, Kaufman YJ (2003) An enhanced contextual fire detection algorithm for MODIS. *Remote Sensing of Environment* **87**, 273–282. doi:10.1016/S0034-4257(03)00184-6

Heward H, Smith AMS, Roy DP, Tinkham WT, Hoffman CM, Morgan P, Lannom KO (2013) Is burn severity related to fire intensity? Observations from landscape scale remote sensing. *International Journal of Wildland Fire* **22**, 910–918. doi:10.1071/WF12087

Hiers JK, O'Brien JJ, Mitchell RJ, Grego JM, Loudermilk EL (2009) The wildland fuel cell concept: an approach to characterize fine-scale variation in fuels and fire in frequently burned longleaf pine forests. *International Journal of Wildland Fire* **18**, 315–325. doi:10.1071/WF08084

Hudak AT, Dickinson MB, Kremens RL, Bright BC, Loudermilk EL, O'Brien JJ, Hornsby B, Ottmar RD (2015*a*) Measurements relating fire radiative energy density and surface fuel consumption – RxCADRE 2011 and 2012. *International Journal of Wildland Fire*. doi:10.1071/WF14159

Hudak AT, Bright BC, Dickinson MB, Satterberg KL (2015*b*) RxCADRE 2008, 2011, and 2012: radiometer locations. Forest Service Research Data Archive (Fort Collins, CO). doi:10.2737/RDS-2015-0035

Johnston JM, Wooster MJ, Lynham TJ (2014) Experimental confirmation of the MWIR and LWIR grey body assumption for vegetation fire flame emissivity. *International Journal of Wildland Fire* **23**, 463–479. doi:10.1071/WF12197

Justice CO, Giglio L, Korontzi S, Owens J, Morisette J, Roy D, Descloitres J, Alleaume S, Petitcolin F, Kaufman Y (2002) The MODIS fire products. *Remote Sensing of Environment* **83**, 244–262. doi:10.1016/S0034-4257(02)00076-7

Justice C, Giglio L, Boschetti L, Roy D, Csiszar I, Morisette J, Kaufman Y (2006) MODIS fire products – algorithm technical background document, version 2.3. Available at http://modis.gsfc.nasa.gov/data/atbd/atbd_mod14.pdf [Verified 10 May 2014]

Justice CO, Román M.O, Csiszar I, Vermote EF, Wolfe RE, Hook SJ, Fried M, Wang Z, Schaaf CB, Miura T, Tschudi M, Riggs G, Hall DK, Lyapustin AI, Devadiga S, Davidson C, Masouka EJ. (2013) Land and cryosphere products from Suomi NPP VIIRS: overview and status. *Journal of Geophysical Research: Atmospheres* **118**, 9753–9765. doi:10.1002/JGRD.50771

Kaufman YJ, Justice CO, Flynn LP, Kendall JD, Prins EM, Giglio L, Ward DE, Menzel WP, Setzer AW (1998) Potential global fire monitoring from EOS–MODIS. *Journal of Geophysical Research* **103**, 32 215–32 238. doi:10.1029/98JD01644

Kremens RL, Dickinson MB (2015) Flame-front scale numerical simulation of wildland fire radiant emission spectra as a guide to wildland fire observation. *International Journal of Wildland Fire* **24**, 461–469. doi:10.1071/WF14036

Kremens RL, Smith AMS, Dickinson MB (2010) Fire metrology: current and future directions in physics-based measurements. *Fire Ecology* **6**, 13–25. doi:10.4996/FIREECOLOGY.0602013

Kremens RL, Dickinson MB, Bova AS (2012) Radiant flux density, energy density, and fuel consumption in mixed-oak forest surface fires. *International Journal of Wildland Fire* **21**, 722–730. doi:10.1071/WF10143

Loudermilk EL, O'Brien JJ, Mitchell RJ, Cropper WP, Hiers JK, Grunwald S, Grego J, Fernandez-Diaz JC (2012) Linking complex forest fuel structure and fire behaviour at fine scales. *International Journal of Wildland Fire* **21**, 882–893. doi:10.1071/WF10116

McKeown D, Cockburn J, Faulring J, Kremens RL, Morse D, Rhody H, Richardson M (2004) Wildfire airborne sensor program (WASP): a new wildland fire detection and mapping system. In 'Remote Sensing for Field Users: Proceedings of the Tenth Forest Service Remote Sensing Applications Conference', 5–9 April 2004, Salt Lake City, UT. (Ed. JD Greer) (CD-ROM) (American Society of Photogrammetry and Remote Sensing: Bethesda, MD)

O'Brien JJ, Loudermilk EL, Hornsby B, Hiers JK, Ottmar RD (2015) High-resolution infrared thermography for capturing wildland fire behaviour – RxCADRE 2012. *International Journal of Wildland Fire* **25**, 62–75. doi:10.1071/WF14165

Ononye AE, Vodacek A, Saber E (2007) Automated extraction of fire line parameters from multispectral infrared images. *Remote Sensing of Environment* **108**, 179–188. doi:10.1016/J.RSE.2006.09.029

Ottmar RD, Hiers JK, Butler BW, Clements CB, Dickinson MB, Hudak AT, O'Brien JJ, Potter BE, Rowell EM, Strand TM, Zajkowski TJ (2015*a*) Measurements, datasets and preliminary results from the RxCADRE project – 2008, 2011 and 2012. *International Journal of Wildland Fire* **25**, 1–9. doi:10.1071/WF14161

Ottmar RD, Hudak AT, Prichard SJ, Wright CS, Restaino JC, Kennedy MC, Vihnanek RE (2015*b*) Pre-fire and post-fire surface fuel and cover measurements collected in the southeastern United States for model evaluation and development – RxCADRE 2008, 2011, and 2012. *International Journal of Wildland Fire* **25**, 10–24. doi:10.1071/WF15092

Peterson D, Wang J (2013) A sub-pixel-based calculation of fire radiative power from MODIS observations: 2. Sensitivity analysis and potential fire weather application. *Remote Sensing of Environment* **129**, 231–249. doi:10.1016/J.RSE.2012.10.020

Peterson D, Wang J, Ichoku C, Hyer E, Ambrosia V (2013) A sub-pixel-based calculation of fire radiative power from MODIS observations: 1 Algorithm development and initial assessment. *Remote Sensing of Environment* **129**, 262–279. doi:10.1016/J.RSE.2012.10.036

Peterson D, Hyer E, Wang J (2014) Quantifying the potential for high-altitude smoke injection in the North American boreal forest using the standard MODIS fire products and subpixel-based methods. *Journal of Geophysical Research: Atmospheres* **119**, 2013JD021067.

Riggan PJ, Tissell RG, Lockwood RN, Brass JA, Pereira JAR, Miranda HS, Miranda AC, Campos T, Higgins R (2004) Remote measurement of energy and carbon flux from wildfires in Brazil. *Ecological Applications* **14**, 855–872. doi:10.1890/02-5162

Roberts G, Wooster MJ, Perry GLW, Drake N, Rebelo LM, Dipotso F (2005) Retrieval of biomass combustion rates and totals from fire radiative power observations: application to southern Africa using geostationary SEVIRI imagery. *Journal of Geophysical Research, D, Atmospheres* **110**. doi:10.1029/2005JD006018

Rowell EM, Seielstad CA, Ottmar RD (2015) Development and validation of fuel height models for terrestrial lidar – RxCADRE 2012. *International Journal of Wildland Fire* **25**, 38–47. doi:10.1071/WF14170

SAS Institute Inc (2013) SAS® 9.4 (SAS: Cary, NC).

Schroeder W, Csiszar I, Giglio L, Schmidt CC (2010) On the use of fire radiative power, area, and temperature estimates to characterize biomass burning via moderate to coarse spatial resolution remote sensing data in the Brazilian Amazon. *Journal of Geophysical Research* **115**, D21121. doi:10.1029/2009JD013769

Schroeder W, Ellicott E, Ichoku C, Ellison L, Dickinson MB, Ottmar R, Clements C, Hall D, Ambrosia V, Kremens RL (2014*a*) Integrated active fire retrievals and biomass burning emissions using complementary near-coincident ground, airborne and spaceborne sensor data. *Remote Sensing of Environment* **140**, 719–730. doi:10.1016/J.RSE.2013.10.010

Schroeder W, Oliva P, Giglio L, Csiszar I (2014*b*) The new VIIRS 375-m active fire detection data product: algorithm description and initial assessment. *Remote Sensing of Environment* **143**, 85–96. doi:10.1016/J.RSE.2013.12.008

Smith AMS, Wooster MJ (2005) Remote classification of head and backfire types from MODIS fire radiative power and smoke plume observations. *International Journal of Wildland Fire* **14**, 249–254. doi:10.1071/WF05012

Val Martin M, Logan JA, Kahn RA, Leung FY, Nelson DL, Diner DJ (2010) Smoke injection heights from fires in North America: analysis of 5 years of satellite observations. *Atmospheric Chemistry and Physics* **10**, 1491–1510. doi:10.5194/ACP-10-1491-2010

Wolfe RE, Nishihama M, Fleig AJ, Kuyper JA, Roy DP, Storey JC, Pratt FS (2002) Achieving sub-pixel geolocation accuracy in support of MODIS land science. *Remote Sensing of Environment* **83**, 31–49. doi:10.1016/S0034-4257(02)00085-8

Wolfe RE, Lin G, Nishihama M, Tewari KP, Tilton JC, Isaacman AR (2013) Suomi NPP VIIRS prelaunch and on-orbit geometric calibration and characterization. *Journal of Geophysical Research, D, Atmospheres* **118**, 11 508–11 521. doi:10.1002/JGRD.50873

Wooster MJ, Zhukov B, Oertel D (2003) Fire radiative energy for quantitative of biomass burning: derivation from the BIRD experimental satellite and comparison to MODIS products. *Remote Sensing of Environment* **86**, 83–107. doi:10.1016/S0034-4257(03)00070-1

Wooster MJ, Roberts G, Perry GLW, Kaufman YJ (2005) Retrieval of biomass combustion rates and totals from fire radiative power observations: FRP derivation and calibration relationships between biomass consumption and fire radiative energy release. *Journal of Geophysical Research: Atmospheres* **110**, D24311. doi:10.1029/2005JD006318

Zajkowski TJ, Dickinson MB, Hiers JK, Holley W, Williams BW, Paxton A, Martinez O, Walker GW (2015) Evaluation and use of remotely piloted aircraft systems for operations and research – RxCADRE 2012. *International Journal of Wildland Fire* **25**, 114–128. doi:10.1071/WF14176

Zhukov B, Lorenz E, Oertel D, Wooster M, Roberts G (2006) Spaceborne detection and characterization of fires during the bi-spectral infrared detection (BIRD) experimental small satellite mission (2001–2004). *Remote Sensing of Environment* **100**(1), 29–51. doi:10.1016/J.RSE.2005.09.019

International Journal of Wildland Fire 25(1) 48–61
doi: 10.1071/WF15090_AC

Supplementary material

Measuring radiant emissions from entire prescribed fires with ground, airborne, and satellite sensors – RxCADRE 2012

Matthew B. Dickinson[A,M], *Andrew T. Hudak*[B], *Thomas Zajkowski*[C,K], *E. Louise Loudermilk*[D], *Wilfrid Schroeder*[E], *Luke Ellison*[F,G], *Robert L. Kremens*[H], *William Holley*[I,L], *Otto Martinez*[I,L], *Alexander Paxton*[I], *Benjamin C. Bright*[B], *Joseph J. O'Brien*[D], *Benjamin Hornsby*[D], *Charles Ichoku*[F], *Jason Faulring*[H], *Aaron Gerace*[H], *David Peterson*[J] *and Joseph Mauceri*[H]

[A]USDA Forest Service, Northern Research Station, 359 Main Road, Delaware, OH 43015, USA.

[B]USDA Forest Service, Rocky Mountain Research Station, Forestry Sciences Laboratory, 1221 South Main Street, Moscow, ID 83843, USA.

[C]USDA Forest Service, Remote Sensing Applications Center, 2222 W. 2300 South Salt Lake City, UT 84119, USA.

[D]USDA Forest Service, Center for Forest Disturbance Science, Southern Research Center, 320 Green Street, Athens, GA 30602, USA.

[E]Department of Geographical Sciences, University of Maryland, College Park, MD 20742, USA.

[F]NASA Goddard Space Flight Center, 8800 Greenbelt Road, Greenbelt, MD 20771, USA.

[G]Science Systems and Applications, Inc., 10210 Greenbelt Road, Suite 600, Lanham, MD 20706, USA.

[H]Rochester Institute of Technology, Center for Imaging Science, 54 Lomb Memorial Drive, Rochester, NY 14623, USA.

[I]US Air Force, 96th Test Wing, Eglin Air Force Base, Niceville, FL 32542, USA.

[J]National Research Council, 7 Grace Hopper Avenue, Monterey, CA 93943, USA.

[K]Present address: Institute for Transportation Research and Education, North Carolina State University, Raleigh, NC 27695, USA.

[L]Deceased.

[M]Corresponding author. Email: mdickinson@fs.fed.us

Accessory publication 1:

Calibration procedure for single-band WASP LWIR data - incorporating spectral sensor response and atmospheric transmission

Matthew B. Dickinson[A,C] *and Robert L. Kremens*[B]

[A]USDA Forest Service, Northern Research Station, 359 Main Road, Delaware, OH 43105, USA.

[B]Rochester Institute of Technology, Center for Imaging Science, 54 Lomb Memorial Drive, Rochester, NY 14623, USA.

[C]Corresponding author: Email: mdickinson@fs.fed.us

We describe a calibration approach providing total ground-leaving radiative excitance (W m^{-2}), also termed fire radiated flux density (FRFD), from the response of a limited-bandpass infrared sensor. The resulting calibration relationships are specific to individual fires because spectral atmospheric transmission data are incorporated. Here we report calibration relationships for the RxCADRE 2011 and 2012 WASP data collections. Calibration of the WASP longwave infrared (LWIR) sensor (8 to 9.2 µm nominal bandpass) (Fig. AP1-1) involves relating total ground-leaving radiance (W m^{-2} sr^{-1}) from 0.1 to 20 µm (accounting for almost all fire radiation) to WASP raw output (digital number, DN) through a number of linked steps. The general calibration equation is

$$L_T = bL_{LWIR}{}^{M} \tag{1}$$

where L_T (W m^{-2} sr^{-1}) is total ground-leaving radiance; L_{LWIR} is detector-reaching radiance in the passband of the WASP LWIR detector during flights over wildland fires; and *b* and *M* are parameters relating restricted-bandpass to total radiance. The inclusion of a unit solid angle in steradians for dimensional consistency is implied (see Palmer and Grant 2009, eq. 2.32). The WASP Indigo Phoenix LWIR camera (model IA126 LWIR) was built by Cantronic Systems Incorporated and has quantum-well, cooled detectors. The WASP LWIR camera has 14 bits of dynamic range and is cooled by a Stirling cooler to about 60°K.

The first step in the calibration process is to relate DN to calculated blackbody radiance in the bandpass of the sensor. For calibration measurements, the blackbody and WASP sensor were placed well off the floor and surrounding areas wrapped in foil to avoid background effects on calibration measurements. The distance between the blackbody and sensor was set so that the blackbody filled more than 40 central pixels. In this near extended–source configuration (NES) (Palmer and Grant 2009, section 7.6.4), the blackbody is close enough to the sensor so that pixels are much smaller than the heated area and radiance reaching the front of the lens is equal to blackbody radiance. The average of pixel DN for a given blackbody temperature is calculated for only the central region of the blackbody where temperatures are uniform. A swing-in blackbody calibrator that is now used during WASP operation and shows that there is minimal drift in DN associated with camera lens temperature variation during flights. The image of the blackbody was flat-fielded to account for known variation in sensor response across the field of view. A 2-ms integration time was used in WASP flight operations in order to avoid saturation yet provide as much background radiance information as possible during fire imaging missions.

Radiance leaving the blackbody and causing a response by the detector (detector-reaching radiance, L_{LWIR}) is a function of blackbody temperature and emissivity along with properties of the sensor. L_{LWIR} is determined over a range of blackbody temperatures (280–1601°K) through integration of Planck's radiation law,

$$L_{LWIR} = \varepsilon t_L \int_0^{\lambda_{max}} f(T, L_\lambda, R_\lambda) \quad (2)$$

where the integral is evaluated from 0 μm to λ_{max} (20 μm), ε is blackbody emissivity (0.95), t_L is proportional transmission of infrared radiation through the lens (0.98), T is blackbody temperature (K), L_λ is spectral radiance (W m^{-2} μm^{-1} sr^{-1}), and R_λ is proportional sensor spectral response (Fig. AP1-1). L_{LWIR} is then related to DN, which is a second-order polynomial in the case of the WASP longwave infrared sensor (Fig. AP1-2):

$$L_{LWIR} = f(DN) = 2x10^{-6}DN^2 + 0.0176DN \quad (3)$$

The parameters b and M relating L_T to L_{LWIR} in Eqn 1 are estimated from the output of 10,000 simulations of total radiative excitance from mixed-temperature fire pixels (Kremens and Dickinson 2014) (Fig. AP1-3). Estimates of total and restricted bandpass (i.e., LWIR) excitance were based on randomly generated assemblages of 30 sub-pixel areas representing the pre-frontal fuel bed, the flaming front, and the zone of post-frontal combustion and cooling. Different sub-pixel areas are defined by their temperatures and emissivities. Total excitance from these sub-pixel areas was calculated from the Stefan-Boltzmann Law and summed to give L_T. L_{LWIR} is calculated as in Eqn 2, but with the additional effect of atmospheric absorption so that it represents WASP LWIR detector-reaching radiance during overflights:

$$L_{LWIR} = \varepsilon t_L \int_0^{\lambda_{max}} f(T, L_\lambda, R_\lambda, A_\lambda) \tag{4}$$

where A_λ is atmospheric spectral transmission calculated from MODTRAN (Table AP1-1, Fig. AP1-4).

Combining Equations 1 and 3 and converting to excitance (W m^{-2}) by multiplication of both sides of the question by π, the form of the final calibration equation for ground-leaving excitance is:

$$P_T = \pi b\big(f(DN)\big)^M \tag{5}$$

where b and M are given in Table 1 for individual fires.

References

Kremens RL, Dickinson MB (2014) Estimating radiated flux density from wildland fires from the raw output of restricted-bandpass detectors. *International Journal of Wildland Fire*, in review.

Palmer JM, Grant BG (2010) 'The art of radiometry.' (SPIE Press: Bellingham, WA). doi:10.1117/3.798237

Table AP1-1. Average atmospheric absorption estimated from MODTRAN for the large 2011 and 2012 burns

Atmospheric profile data used in MODTRAN are from soundings collected from balloons launched before ignition. Relative humidity is averaged from the surface to 3000 m. Flight altitude used was representative of the VIIRS and MODIS overpass times. Parameters *b* and *M* from Eqn 1 are estimated from a power-law fit to untransformed data because this approach, in contrast to linear regression on log-log transformed data, resulted in the least bias in background fire radiative flux density (FRFD)

Fire	Date	Launch time (UTC)	Air temperature (°K)	Relative humidity (%)	Ignition time (UTC) Start	Ignition time (UTC) End	Flight altitude (m)	Average transmission (8-9.2 μm)	b	M
703C	06 February 2011	15:00	280	28	18:24	19:02	3030	0.88	5.216	1.374
608A	08 February 2011	14:50	285	37	18:25	19:55	2250	0.90	5.138	1.374
L1G	04 November 2012	20:31	300	48	18:30	19:46	3155	0.71	7.282	1.393
L2G	10 November 2012	20:10	296	47	18:03	21:00	3160	0.75	7.006	1.380
L2F	11 November 2012	21:49	297	50	18:23	19:05	1550	0.76	6.718	1.385

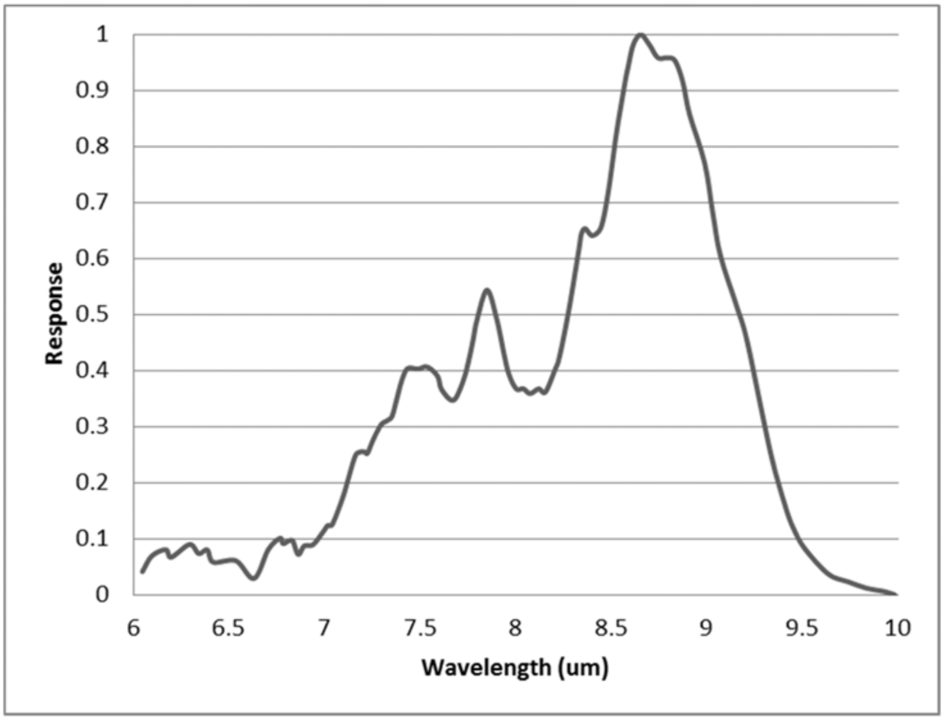

Fig. AP1-1. Spectral response of the WASP longwave infrared sensor. The nominal bandpass of the sensor is 8–9.2 µm, approximately the full width of the spectral response at 50% response (full width at one-half maximum) (FWHM).

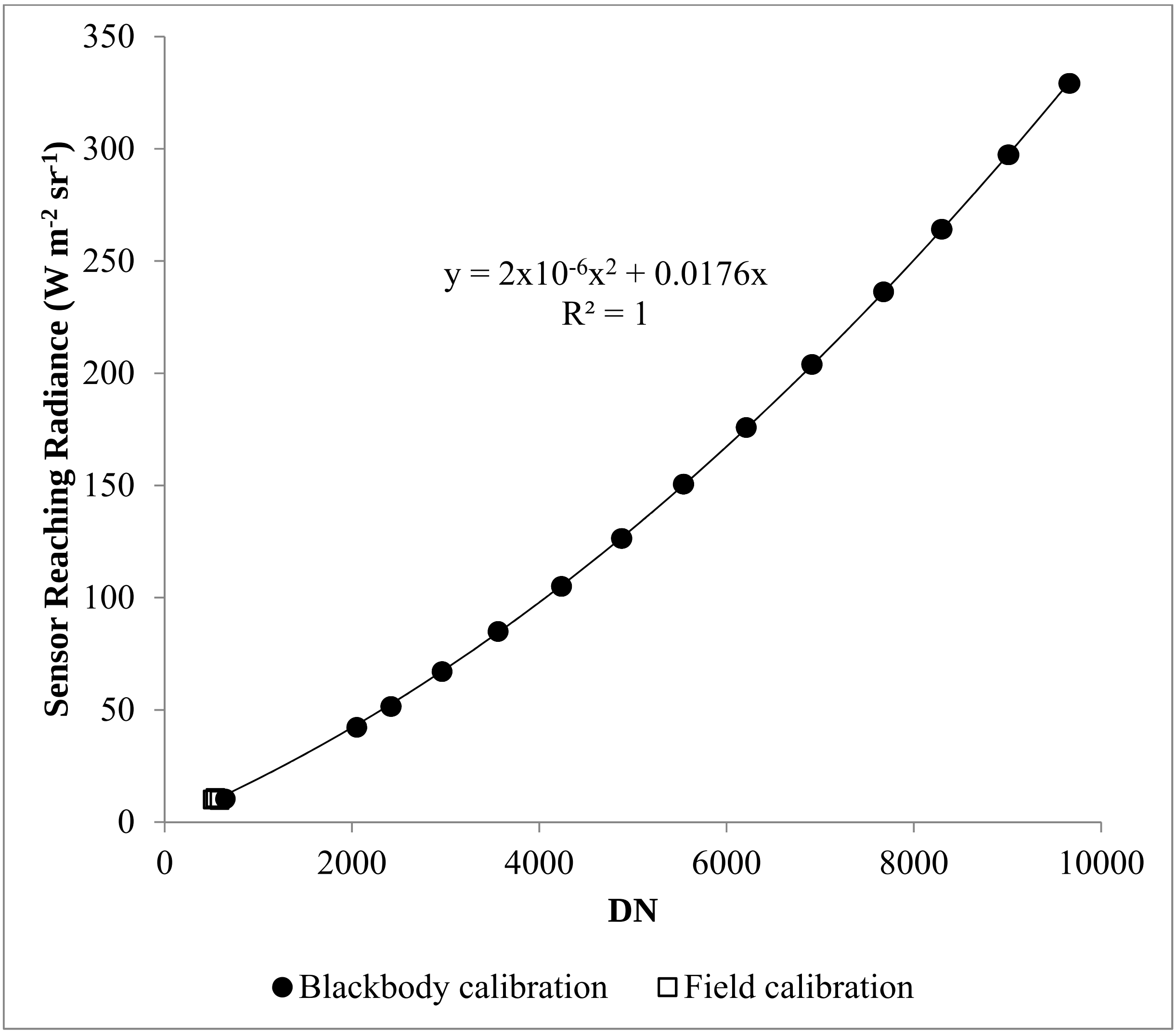

Fig. AP1-2. Calibration relationship for radiance in the WASP longwave infrared passband determined from laboratory blackbody calibration (closed circles) and three field measurements (open circles). Field measurements are average WASP background DN during three fires and detector-reaching radiance estimated for the WASP passband at the observed air temperature (see above). The polynomial regression fit only included blackbody data.

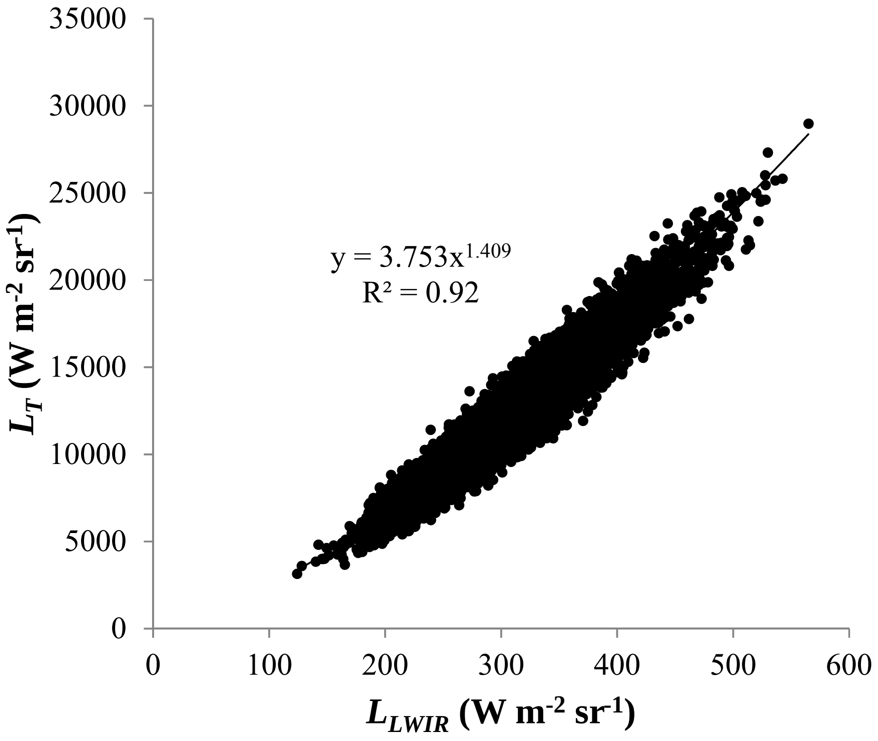

Fig. AP1-3. Power-law relationship between untransformed (total) ground-leaving and detector-reaching radiance for L2F from 10,000 fire pixel simulations. Results for other fires were similar (Table 1).

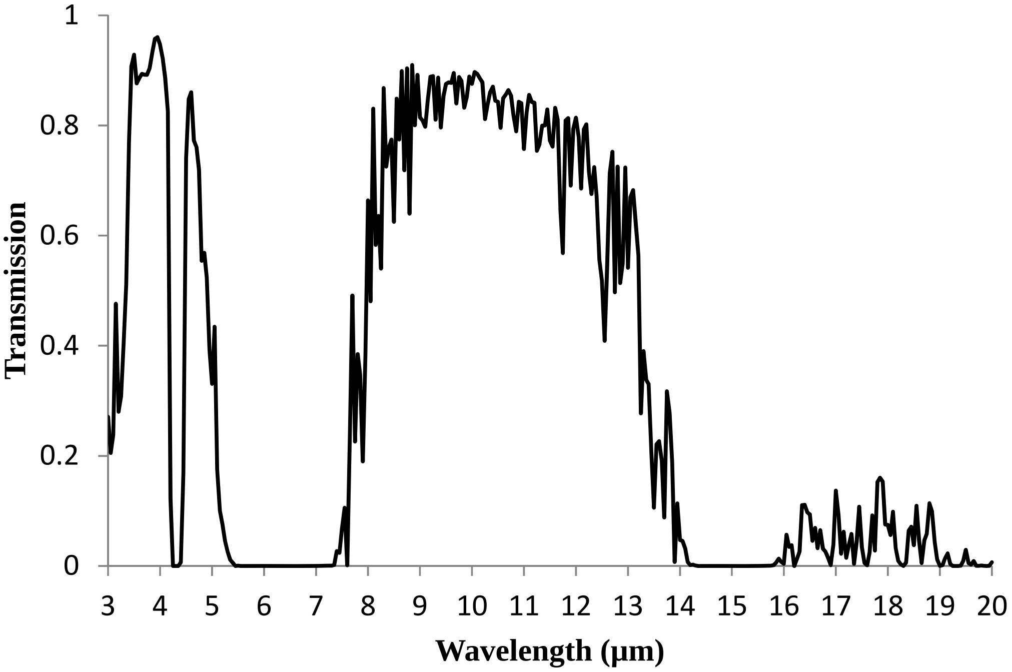

Fig. AP1-4. MODTRAN spectral atmospheric transmission for L2F based on an atmospheric profile from a mid-morning sounding conducted prior to ignition (see Table AP1-1).

Accessory publication 2:

Alternative methods for estimating fire radiated power from MODIS observations when fire boundaries are known

Luke Ellison[A,B,C] and *Charles Ichoku*[A]

[A]NASA Goddard Space Flight Center, 8800 Greenbelt Road, Greenbelt, MD 20771, USA.

[B]Science Systems and Applications, Inc., 10210 Greenbelt Road, Suite 600, Lanham, MD 20706, USA.

[C]Corresponding author: Email: luke.ellison@ssaihq.com

MODIS fire detections were obtained from the MYD14 active fire product (e.g., Giglio et al. 2003) and, of the four coincident MODIS overpass events for RxCADRE 2012 burns (S6, L1G, L2G and L2F), only two (L2G and L2F) were represented in MYD14. MODIS detected two fire pixels for the L2G burn with fire radiated power (FRP) totaling 130.9 MW, and three fire pixels from one complete scan for the L2F burn totaling 151.9 MW (see Table AP2-1, row 1). The S6 burn signal was too small to be detected in the significantly-off-nadir MODIS pixels as can be seen in Fig. AP2-1. Although the MYD14 algorithm detected an elevated signal for the L1G burn, it classified it as cloud due to the significant cloud cover over or near the fire (see Fig. AP2-1). However, in spite of the extensive cloud cover, knowing that the detected signal was indeed from the L1G fire provided the rationale to utilize the available data to retrieve FRP. This was done and a cumulative total FRP of 110.8 MW was found over four pixels for the L1G burn (Table AP2-1, row 1). The extent of attenuation of FRP by cloud cover is unknown.

In an effort to get the most realistic estimates of FRP possible, different methodologies for calculating FRP from the MODIS data were implemented for the fires. For each burn, FRP was calculated in two modes: by summation of the individually retrieved fire detections, and by clustering together all of the MODIS pixels touching the burn blocks prior to FRP retrieval (Table AP2-1, column 'Mode'). In addition to using the MYD14 default background characterizations, the small number of burns in this experiment allowed us the flexibility to manually inspect the background pixels of the MODIS fire detections. This was done to ensure that any non-clear background pixels were properly excluded from the analysis (Table AP2-1, column 'Background'). The fact that the differences between rows 1 and 3 and between 2 and 4 in Table AP2-1 are relatively small corroborates the clustering methodology. These small differences are due to the different order of calculations and the slightly different selection of background pixels. Thus, for L1G that has a high level of cloud contamination in the background, the difference between the pixel and cluster modes using the default background characterization is greater than the others. Having corroborated the clustering technique, more complete FRP values could be obtained by clustering all the pixels containing any portion of the burn plot on the ground (Table AP2-1, column 'Cluster Size').

The official MYD14 product corresponds to the first row of Table AP2-1, although the value for L1G was not available in the product but was calculated in this study based on the MYD14 algorithm. When a manual inspection of the background was done to ensure that none of the selected background pixels were contaminated (by clouds, water, smoke, significant shadows, etc.), the FRP values for L2G and L2F remained in close agreement with the MYD14 product (Table AP2-1, row 2). However, the stricter manual implementation of cloud detections yields a noticeable decrease in FRP for L1G to 94.4 MW. This value is an underestimate of L1G FRP because, although the background was properly classified, the fire pixels still contain many clouds that lower the fire signal. Because we have confidence in the clustering method (see above), we used this method to calculate FRP for all pixels that overlap the burn blocks (see Fig. AP2-1). The clustering method yields values shown in Table AP2-1, rows 5 and 6, that are significantly higher than the corresponding prior estimates. Note that the cluster analysis was not successful for L1G in this case due to the great variability in brightness temperatures of pixels covering the fire because of the extensive cloud cover in that area. Therefore, the inclusion of non-detected parts of a fire can mitigate satellite underestimation of the whole-fire FRP output. We have the greatest confidence in the FRP estimates that are derived from the cluster method and that manually select background pixels. These FRP estimates are 151.4 MW for L2G and 174.6 MW for L2F. Due to the increased uncertainty in the L1G case from cloud attenuation of the fire signal that prevented FRP estimation using the whole-fire clustering technique, we can state with confidence only that FRP from L1G was greater than 94.9 MW.

References

Giglio L, Descloitres J, Justice CO, Kaufman YJ (2003) An enhanced contextual fire detection algorithm for MODIS. *Remote Sensing of Environment* **87**, 273–282. doi:10.1016/S0034-4257(03)00184-6

Table AP2-1. FRP values generated using different methodologies from MODIS data for the L1G, L2G and L2F burns

Each method can be described by its FRP-retrieval 'mode', background characterization, and by cluster size (if applicable). Under the 'Mode' column, 'pixels' denote hot spot determination of individual pixels followed by aggregation of their FRP values, whereas 'cluster' denotes pixel aggregation covering the fire followed by a single FRP retrieval for the whole cluster. Under the 'Background' column, 'default' denotes when the default MYD14 characterizations are used to select the background, and 'manual' denotes when the background pixels are manually selected. Under the 'Cluster Size' column, 'default' refers to the use of only pixels flagged as fire in the 'pixels' Mode, and 'all' refers to the use of all pixels that include any portion of the burn block on the ground (see Fig. AP2-1)

Methods of generating FRP			Fire radiated power		
Mode	Background	Cluster size	Burn unit		
			L1G	L2G (MW)	L2F
Pixels	Default	–	110.8	130.9	151.9
Pixels	Manual	–	94.4	130.1	155.6
Cluster	Default	Default	123.8	134.7	160.8
Cluster	Manual	Default	94.9	133.7	158.5
Cluster	Default	All	149.6	152.6	179.1
Cluster	Manual	All	–	151.4	174.6

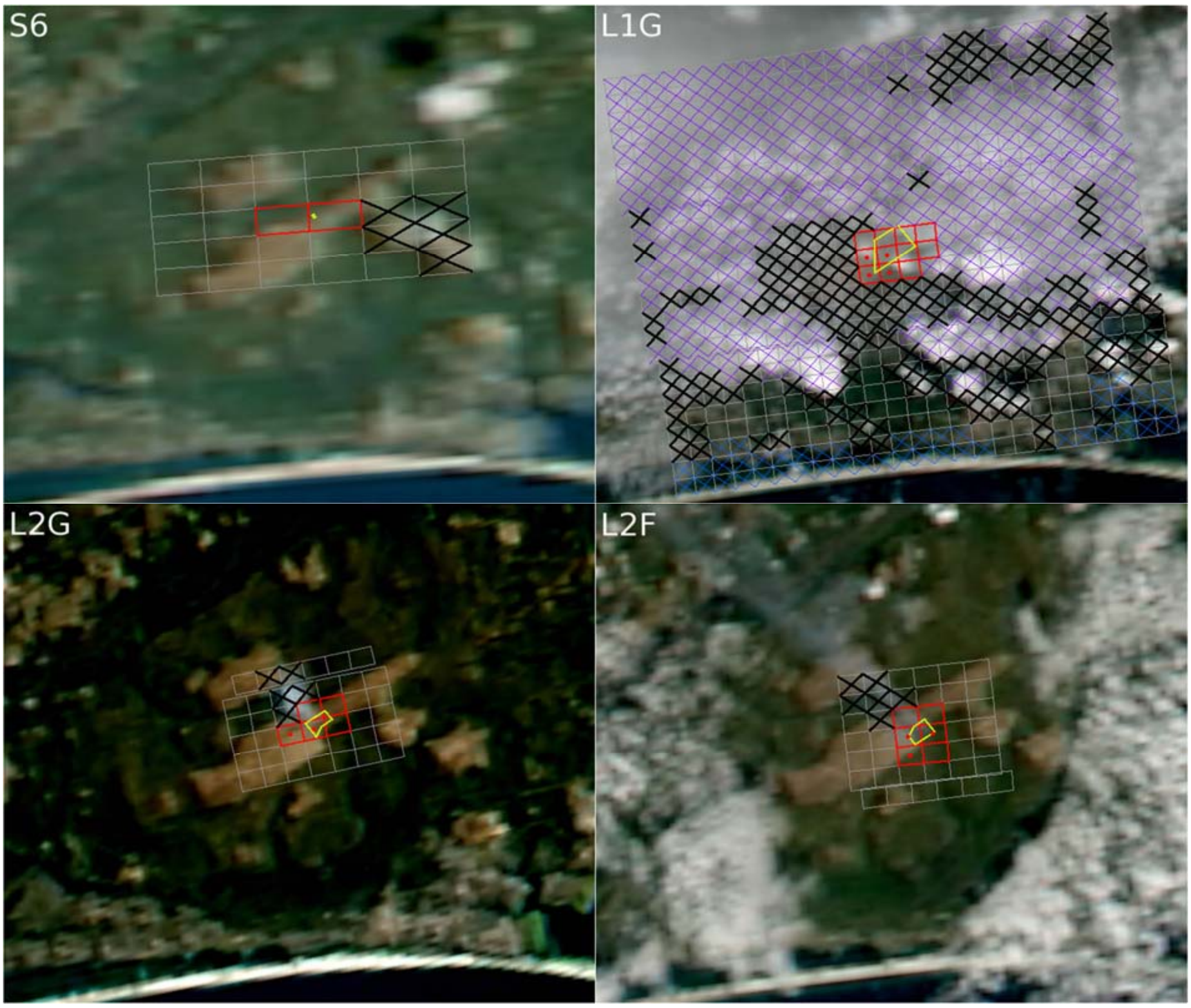

Fig. AP2-1. Diagrams of the MODIS 1-km pixels superimposed on MODIS 250-m imagery for units S6, L1G, L2G and L2F. The burn blocks are outlined in yellow, and the MODIS pixels that cover all or a portion of the burn block, keeping in mind the MODIS triangular response function that reaches halfway into the neighboring pixels along-scan, are outlined in red (Table AP2-1, rows 5 and 6). Individual pixels whose signals were strong enough to be deemed as fire detections are shown with a red dot (Table AP2-1, rows 1 and 2). Pixels excluded from the background characterization are 'X'ed out: clouds are shown in purple, water is shown in blue, and user-selected contaminated pixels are shown in thick black.